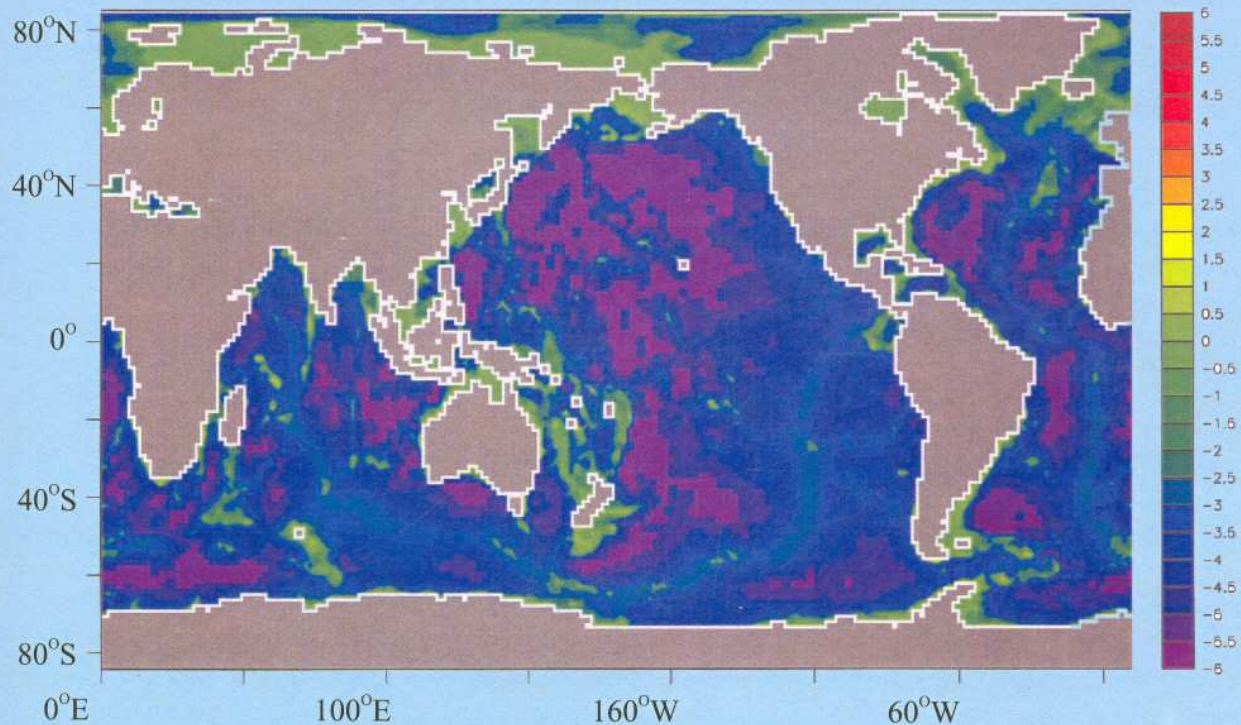


Time - mean Oceanic Response and Interannual Variability in a Global Ocean GCM Simulation



K.V. Ramesh and R. Krishnan

September 2003



**Indian Institute of Tropical Meteorology
Pune - 411 008, India**

ISSN 0252-1075
Contribution from IITM
Research Report No. RR-100

Time-mean Oceanic Response and Interannual Variability in a Global Ocean GCM Simulation

K.V. Ramesh
and
R. Krishnan

September 2003



Indian Institute of Tropical Meteorology

Dr. Homi Bhabha Road, Pashan Pune - 411 008
Maharashtra, India

E-mail : lip@tropmet.ernet.in
Web : <http://www.tropmet.ernet.in>

Fax : 91-020-5893825
Telephone : 91-020-5893600

Contents

Abstract	i
1 Introduction	1
1.1 Brief description of ocean model	3
1.1.1 Initialization and spin-up	3
2 Analysis of time-mean features	5
2.1 Simulation of SST	5
2.2 Vertical stratification	6
2.3 Meridional heat transport	6
3 Interannual variability	8
3.1 Temperature variability	8
3.2 SSH variability	9
4 Analysis of ENSO	9
4.1 Description of ENSO simulation	10
4.2 Life cycle	11
4.3 Physical interpretation of the model ENSO	12
5 Meridional heat transport during ENSO	15
6 Summary	18
A Heat flux calculations	20
B References	21
C Figures	25

Time-mean oceanic response and interannual variability in a global ocean GCM simulation.

K.V. Ramesh and R. Krishnan

Indian Institute of Tropical Meteorology, Pune 411 008, India.

ABSTRACT

A 43-year (1958-2000) numerical simulation is performed using a state-of-the-art global ocean general circulation model (OGCM); along with supplementary diagnostic analysis of multi-source datasets in order to investigate aspects concerning the mean structure and interannual variability associated with the ocean response to atmospheric forcings. The OGCM simulation is found to be consistent with observed datasets in bringing out the time-mean features and the interannual variability of large-scale oceanic circulations and more specifically the major El Niño / Southern Oscillation (ENSO) events during the 43-year period. The life cycle of the model ENSO shows that the long-term memory of the phenomenon arises from the evolution of the subsurface ocean anomalies. Further, the findings reveal that the equator-to-pole heat transport in the Pacific Ocean tends to vary significantly during ENSO. In particular, the poleward heat transport typically increases during El Niño episodes by as much as 1.2×10^{15} Watts from its mean value. The OGCM simulation shows that the ENSO related upwelling changes and temperature anomalies in the equatorial thermocline are accompanied by coherent circulation changes in the subtropics as well. The anomalous northward currents linking the equator and subtropics appear as deep as 250m and reduce the equatorward transport of cold subsurface water from the subtropics by nearly 3.4 Sv during El Niño events, thereby providing a mechanism for preventing accumulation of excessive heat and mass near the equator. While observational estimates of time-dependent ocean heat transport have been fragmentary, the above results raise the possibility that dynamical interactions between the equatorial and subtropical Pacific Ocean could be important in determining the ENSO evolution itself.

1 Introduction

Oceans form a vital component of the climate system. On account of the high thermal capacity of sea water and the slow variations of the oceanic currents, the large-scale response in the world oceans is typically associated with timescales that are much longer than those of the atmosphere. Variations in the heat storage of the ocean manifest as anomalies in the sea-surface and subsurface temperature field that are in turn related to dynamical changes in the structure of the upper ocean. Oceans also play a major role by transporting heat from the tropics to the high latitudes. Estimates of the time-mean meridional transport of heat by the oceans are of the same order as the atmosphere (Jayne and Marotzke, 2001). Hence accurate model simulation of the vertical stratification and the meridional heat transport of the world oceans is an essential pre-requisite for climate modeling (Hu, 1997). Besides the mean state, the processes that contribute to the variability of the atmosphere-ocean system are also of great interest in understanding the evolution of climatic anomalies on seasonal, interannual and longer time-scales (Lau, 1997). Slow variations of sea-surface temperature (SST) serve as boundary forcing for generating persistent atmospheric anomalies. Therefore, efforts toward reliable predictions of future climate warrant realistic simulation of both the mean state as well as the variability of the global oceans.

Given the sparsity of oceanic observations, several aspects of the 3-dimensional structure and evolution of oceanic circulations are not adequately known. Therefore, ocean general circulation models (OGCM) provide atleast first-order estimates of various parameters at the surface and the interior of the global oceans. OGCMs capable of simulating the full 3-dimensional ocean circulation with realistic bottom topography have been available since the 1970's (eg., Semtner and Chervin, 1988, Semtner, 1995). Developments in satellite observing systems along with improvements in numerical modeling and supercomputer technology have made significant strides in our ability to observe and model the global ocean circulation (Fu and Smith, 1996). Numerous studies over the last two decades and the success of the Tropical Ocean Global Atmosphere (TOGA) program have considerably advanced our understanding of El Niño / Southern Oscillation (ENSO) and laid the foundations of tropical ocean-atmosphere interactions (Wallace *et al.*, 1998; Neelin *et al.*, 1998; McPhaden *et al.*, 1998). The theory that ENSO arises as a natural

mode of the tropical coupled ocean-atmosphere system dates back to the hypothesis of Bjerknes (1969). The essence of Bjerknes's postulate, as reinterpreted in the light of the current knowledge, is that ENSO arises as a self-sustained cycle in which anomalies of SST in the Pacific cause the trade winds to strengthen or slacken and this in turn drives the ocean circulation changes that produce anomalous SST (Neelin et al., 1998). Several studies have reported the occurrence of such self-sustained oscillations of the coupled ocean-atmosphere system in model simulations (Philander et al., 1984; Yamagata, 1985; Cane and Zebiak, 1985; Hirst, 1986; Zebiak and Cane 1987 and many others).

Despite the above studies, various aspects relating to the evolution of ENSO are not fully understood. For instance, it is not known how the meridional heat transport in the oceans is affected during El Niño and La Niña events. This is partly because of the lack of observations of the time-dependent variations of meridional heat transport. Model calculations of heat transport in the Pacific Ocean are relatively few (Bryan, 1982; Meehl *et al.*, 1982) and these studies mostly describe the seasonal cycle of heat transport. In a recent paper, Sun (2000) analyzed the heat balance of the coupled tropical ocean-atmosphere system using the data from the Earth Radiation Budget Experiment (ERBE), atmospheric circulation statistics from NCEP reanalysis and upper ocean heat content from ocean data assimilation. His study indicated a substantial increase in the meridional heat transport in the tropical Pacific Ocean during the 1986-87 El Niño. The ERBE dataset period (1985-89) contains only one El Niño event. Moreover the convergence of heat in the upper ocean computed by Sun (2000) was based on a 1-dimensional energy balance model and did not explicitly include ocean internal dynamics. In an important work, Bryan (1982) demonstrated that variations in the zonal component of the wind stress play a major role in affecting the oceanic meridional circulation and the associated poleward heat transport. While it is well-known that the ENSO cycle is accompanied by significant changes in the surface easterly trade winds over the tropical Pacific, it is not adequately clear as to how the poleward heat transport in the Pacific Ocean responds to the ENSO related atmospheric forcings. In particular, the linkage between ENSO and the interannual variations of heat transport and associated variability in the subtropical Pacific Ocean is not obvious. Keeping these issues in mind, we have performed a 43-year integration of a full 3-D OGCM driven by atmospheric forcings and validated the OGCM simulations with oceanic datasets from multiple sources. These include SST

data from GISST2.3b dataset (Rayner *et al.*, 1994); potential temperature and salinity from the World Ocean Atlas98 (Levitus, 1994 a,b) and also from the GFDL assimilation monthly dataset (GFDLAD) based on Derber and Rosati (1989) for the period (1980-99); subsurface temperature observations from the Tropical Atmosphere Ocean (TAO) moored buoys (McPhaden, 1998); and sea surface height (SSH) from TOPEX/POSEIDON (T/P) dataset (ftp://podaac.jpl.nasa.gov/pub/data_collections/monthly_mean_atlas). Additionally, the meridional heat transport computed using the potential temperature and current data from GFDLAD dataset is used for validating the OGCM simulation. The details of the OGCM simulation experiment are given below.

1.1 Brief description of ocean model

The OGCM used in our study is the reformulated version of the Bryan-Cox-Semtner (BCS) model (Bryan, 1969), developed at the Los Alamos National Laboratory (LANL) under the Parallel Ocean Program (POP) (Smith *et al.*, 1992; Dukowicz *et al.*, 1993) and has been designed to run efficiently on massively parallel machines. The reformulated barotropic equations in the OGCM are represented in terms of the surface pressure formulation (Dukowicz and Smith, 1994) rather than volume-transport streamfunction originally used in BCS models. In addition to being computationally efficient, this method has several other advantages: (a) any number of islands can be included in the computational grid at no extra cost (b) the model can handle steep gradients in the bottom topography (c) free-surface height is a prognostic variable. The model formulation is described in Smith *et al.*, (1992) and Dukowicz *et al.*, (1993). Several aspects of ocean circulation dynamics are known to be simulated realistically by the POP OGCM both on global (Fu and Smith, 1996; Maltrud *et al.*, 1998) and regional (Smith *et al.*, 2000) scales.

1.1.1 Initialization and spin-up

The present OGCM has intermediate resolution with horizontal longitude-latitude grid spacing of $1.875^\circ \times 1.406^\circ$ and 32 nonuniform vertical levels, which vary in thickness from about 10m at the surface to 500m in the deeper regions. The 32 vertical levels in the model correspond to (5, 15, 25, 35, 50, 75, 100, 125, 150, 200, 250, 300, 400, 500, 600, 700, 800, 900, 1000, 1100, 1200, 1300, 1400, 1500, 1750, 2000, 2500, 3000, 3500,

4000, 4500, 5000) in meters. Using the high-resolution (0.08°) WORLDBATH - 432 data (<http://ingrid.ldeo.columbia.edu/SOURCES/.WORLDBATH>), we generated a realistic bottom topography and regridded to the model resolution (figure not shown). We used this model topography field to build a 3-dimensional land-sea mask parameter at each (x,y,z) co-ordinate of the model domain. A Laplacian form of diffusion scheme is used to represent horizontal mixing of heat, salt and momentum. The horizontal diffusion coefficient for heat and salt is taken to be $2 \times 10^7 \text{ cm}^2\text{s}^{-1}$ and the horizontal viscosity coefficient is taken to be $2 \times 10^7 \text{ cm}^2\text{s}^{-1}$. Although, the horizontal diffusion coefficient and horizontal viscosity coefficient are chosen to have the same value in our numerical simulations, in general they can be different. The diffusion and viscosity coefficients are determined taking into consideration the model resolution (Bryan, 1969). The vertical friction and diffusion involve Richardson number-dependent mixing coefficients (Pacanowski and Philander, 1981). The vertical diffusion coefficient of heat and salt is $0.1 \text{ cm}^2\text{s}^{-1}$ and the corresponding viscosity coefficient is taken to be $1.0 \text{ cm}^2\text{s}^{-1}$.

In order to attain a quasi-equilibrium state, the OGCM was initially spun-up in a 24 year integration carried out in 4 stages. The spin-up procedure adopted by us is similar to that of Semtner and Chervin (1988). Beginning from a state of rest, we initialized the potential temperature (Θ) and salinity (S) fields in the ocean to the observed annual mean values obtained from the WOA98 dataset originally developed by Levitus (1994a,b). In the first stage, the OGCM was forced by observed monthly climatological wind stress (Hellerman and Rosenstein, 1983) and integrated for 8-years. Here, the (Θ , S) fields at the surface were restored to their observed monthly climatological values; while the interior values of (Θ , S) were restored to their annual mean values. In the second stage, the model was integrated for 4 more years by slowly restoring the interior (Θ , S) fields with restoration time-scale ~ 3 -years. This slow restoration produces a relatively balanced state of the ocean circulation. In the third stage, the model was integrated for another 4 years by using monthly climatological interior (Θ , S) fields in order to allow the mesoscale eddies to attain realistic energy levels. In the final phase of the spin-up, the model was integrated for 8 years by removing the interior forcing and allowing the interior fields to freely evolve. The forcing during the last 4 years of the final phase uses monthly climatological wind-stress and heat fluxes computed from National Center for Environmental Prediction (NCEP) reanalysis (Kalnay *et al.*, 1996; Kistler *et*

al., 2001) available for the period (1958 - 2000). The time-variation of global mean kinetic energy (GMKE) during the 24-year spin-up period is shown in Fig.1. Initially the kinetic energy increases and later drops to around $6.0 \text{ cm}^2\text{s}^{-2}$ in about three years. This value is steadily maintained till about 16 years. Due to withdrawal of the interior forcing, the GMKE further decreases to about $4.0 \text{ cm}^2\text{s}^{-2}$ during the last 8 years of the spin-up. The magnitude of GMKE is similar to that obtained by Dukowicz and Smith (1994) at the end of their model spin-up. The ocean condition at the end of the 24-year integration is considered to be the quasi-equilibrium state. After the model spin-up, we have performed a 43-year (1958-2000) integration of the OGCM, driven by wind-stress and the heatflux forcings computed from NCEP reanalysis. The surface heatflux forcing computations are described in Appendix A.

2 Analysis of time-mean features

One of the criteria to infer the reliability of OGCM simulations is to assess the model's ability to realistically capture the time-mean state and seasonal evolution of sea surface temperature (SST), the vertical structure of temperature, salinity and the meridional heat transport. We shall now examine the time-mean simulation of these oceanic parameters and validate with various datasets.

2.1 Simulation of SST

The OGCM simulation of mean SST for January and July months is shown in Fig.2a and Fig.2b respectively. The corresponding observed SST from WOA98 are shown in Fig.2c and Fig.2d respectively. Note that the distribution of warm SST in the tropics and cold SST in the extra-tropics simulated by the model is consistent with the observed SST distribution. The SST in the west Pacific warm pool region seems to be slightly overestimated in the model as compared to WOA98. Nevertheless, the seasonal variation of SST is conspicuously seen in the tropical Pacific, Indian and Atlantic Oceans both in the OGCM simulation and the observed SST. By comparing the model and Levitus WOA98 SSTs month-by-month for different ocean basins, we have separately verified the correspondence between the two datasets. The root-mean-square (RMS) difference between the OGCM and Levitus monthly SSTs is found to be typically around 0.14

$^{\circ}\text{C}$ for the tropical Indian Ocean; 0.28°C for the tropical Pacific Ocean and 0.23°C for the tropical Atlantic Ocean (figure not shown). The RMS difference for the global mid-latitude SST is found to be less than 0.45°C . We have also verified that several large-scale circulation features such as the westward surface currents in the equatorial Pacific, Indian and Atlantic Oceans; the subtropical gyres in the Pacific, Atlantic and South Indian Oceans; the Antarctic Circumpolar Current and the western boundary currents (*eg.*, Gulf stream, Kuroshio, etc.) are captured in the OGCM simulation (figure not shown).

2.2 Vertical stratification

Latitude-depth sections of zonally averaged (Θ , S) are useful for understanding the vertical stratification in the oceans (Hu, 1997). It can be noted from Figs.3(a-c) that the equator-to-pole temperature gradient is very prominent in the top 500 meters of the ocean. The temperature at 500m is about 6°C in Figs.3(a-c). The vertical stratification of temperature is more clearly seen in the subtropics as compared to the equatorial region. This is in association with stronger subsidence in the subtropical oceans. The salinity sections in Figs.3(d-f) consistently show higher salinity in the subtropics as compared to the equatorial oceans. It is also realized that there are some shortcomings in the OGCM simulation. For instance, the salinity distribution in the OGCM seems to be underestimated in the subtropics; while it is somewhat higher in the equatorial region, as compared to the WOA98 and GFDLAD datasets. Also the OGCM simulation shows differences in the salinity distribution in the high latitude regions as compared to the other two datasets. Nevertheless, it can be seen from Fig.3 that the gross features of the vertical stratification in the OGCM simulation show overall consistency with the WOA98 and GFDLAD datasets.

2.3 Meridional heat transport

Covering 71% of the Earth's surface, the oceans absorb nearly twice as much of the sun's radiation as the atmosphere. With their huge heat capacity, the oceans damp temperature fluctuations; in addition they play a more active and dynamic role in the heat balance of the climatic system. In order to maintain the heat balance in the oceans, huge amount of heat is transported from the equator to the poles. Estimates of the net time-mean ocean

heat transport show that the ocean carries the same order of magnitude of energy towards the poles as the atmosphere (Vondere Haar and Oort, 1973; Hastenrath, 1982; Peixoto and Oort, 1992; Keith, 1995; Trenberth *et al.*, 2000, Jayne and Marotzke, 2001). However in contrast to the atmosphere, the oceans are confined by land masses, so that their heat transport is channelled into specific regions. The net effect is to transport heat from the equator to the polar regions along the west sides of the ocean basins and to transport cold water from polar regions towards the equator. Figure 4 shows the seasonal and annual cycle of heat transport for individual ocean basins (Pacific, Indian and Atlantic Oceans) in the OGCM simulation (left panel) and the GFDLAD dataset (right panel). The net northward heat transport is directly computed from the potential temperature (Θ) and meridional velocity (v) fields as follows: $Q = \rho_o c_p \int \int v \Theta \, dx \, dz$ where Q is the heat transport, ρ_o ($= 1025 \, \text{kg m}^{-3}$) is mean density of sea water; c_p ($= 3994 \, \text{J kg}^{-1} \, \text{C}^{-1}$) is the specific heat capacity of water (Jayne and Marotzke, 2001).

It can be seen from Fig.4 that the seasonal meridional heat transport in the tropics is largely from the Pacific and Indian Oceans; but is small for the tropical Atlantic Ocean. The peak northward transport in the tropics during January (July) in the OGCM simulation is about 3.8 PW (-3.4 PW) for the World Ocean; 2.4 PW (-1.7 PW) for the Pacific Ocean; 1.6 PW (-1.7 PW) for the Indian Ocean ($1 \, \text{PW} = 10^{15} \, \text{Watts}$). The above values compare well with the estimates of Jayne and Marotzke (2001). Note that the maximum northward transport during winter months occurs around 9°N in the Pacific Ocean and around 10°S in the Indian Ocean. During summer, the maximum southward transport is seen around 10°S in the Pacific Ocean and around 14°S in the Indian Ocean. Furthermore, the heat transport in the Southern Indian Ocean shows a secondary peak near 30°S with net northward transport of about 2.0 PW both in the winter and summer months. It is important to note that the annual cycle of meridional heat transport is prominent mostly in the tropical Pacific and Indian Oceans. The OGCM shows very little seasonal variation in the meridional heat transport for the Atlantic Ocean. The annual cycle of heat transport in the OGCM shows a peak northward heat transport of 5.98 PW for the World Ocean; 3.2 PW for the Pacific Ocean and 2.8 PW for the Indian Ocean. The above OGCM estimates are in good agreement with those obtained by Jayne and Marotzke (2001) - 6.2 PW (World Ocean), 3.0 PW (Pacific Ocean) and 3.0 PW (Indian Ocean). Also the OGCM heat transport estimates are comparable with those computed

from the GFDLAD dataset - 7.1 PW (World Ocean), 3.67 PW (Pacific Ocean) and 3.0 PW (Indian Ocean).

3 Interannual variability

Using the 43-year integration, we shall now examine the interannual variability of the OGCM response to interannually varying atmospheric forcings.

3.1 Temperature variability

Interannual changes in the oceanic response, to varying surface windstress and heat flux forcings, manifest as anomalies in the surface and subsurface temperatures and are useful indicators of air-sea coupling. The plot in Figs.5(a-c) shows the spatial map of standard deviation of ocean temperatures, computed from the 43-year (1958-2000) OGCM simulation, at three vertical levels (5m, 100m, 150m). The region of largest temperature variability at the 5m level is seen in the equatorial Pacific extending eastward from 150°E up to the west-coast of South America. The maximum standard deviation in the eastern equatorial Pacific is about 1.2°C and indicates the oceanic signature of ENSO. A secondary maximum of SST variability is seen in the central and eastern tropical Indian Ocean. In addition, the SST variability is significant in the mid-latitude regions of North Pacific and western part of North Atlantic Ocean. Earlier studies indicate that the variability in the North Pacific is associated with anomalies in heat flux and surface winds (Cayan, 1980, Deser and Blackmon, 1995, Ronca and Battisti, 1997). The temperature variability at 100m (Fig.5b) and 150m (Fig.5c) shows that the subsurface variations are more pronounced in the tropical west Pacific, where the thermocline is deep. On the other hand, the subsurface variability is small in the eastern equatorial Pacific. This feature is consistent with the observed subsurface temperature variability described by Lysne and Deser (2002). The subsurface variability in the west Pacific shows off-equatorial maxima located around 10° latitude on either side of the equator. The maximum value at 100m is about 1.2°C and about 1.5°C at 150m. In addition to the Pacific basin, the variability of subsurface temperatures can also be seen in the equatorial and North Atlantic Ocean.

3.2 SSH variability

Atmosphere-ocean interactions not only affect the ocean temperatures but also produce large-scale variations in mean sea level. The ability of the POP model to simulate the observed SSH variability has been documented by earlier studies (Fu and Smith, 1996). Sea surface height is a prognostic variable in the present OGCM. The standard deviation of SSH from the T/P dataset and that from the 43-year OGCM simulation are shown in Fig.6a and Fig.6b respectively. It can be seen from Fig.6 that the dominant SSH variability occurs in the west Pacific region. Note that the two off-equatorial maxima of in the west Pacific are co-located with the pattern of temperature variability described previously in Figs.5(b-c). The southern tropical Indian Ocean also shows significant SSH variations as evident from Figs.6(a-b). The SSH variability in the OGCM seems to be weaker in the central-eastern equatorial Pacific as compared to the T/P dataset. Likewise, the SSH variability in the western part of North Pacific and North Atlantic Oceans seem to be underestimated in the OGCM relative to the T/P dataset. It must be pointed out that the T/P dataset is available at a much higher spatial resolution (0.1°) and therefore captures finer details of mesoscale oceanic eddies. Moreover, the OGCM is driven by monthly forcings and therefore much of the high-frequency (≤ 1 month) variability is damped in the OGCM. Nevertheless, the overall pattern of SSH and subsurface temperature variability in the tropical oceans (Fig.6 and Fig.5) indicates that the circulation variability at the surface is dynamically coupled to the subsurface variability.

4 Analysis of ENSO

The ENSO phenomenon represents a natural mode of variability of the tropical atmosphere-ocean coupled system and is a major contributor to interannual time-scale climate anomalies world-wide (Wallace, *et al.*, 1998). This is the reason for focusing on the ENSO simulation in the OGCM. Numerous theoretical and modelling studies have investigated the physical mechanisms of ENSO (Cane and Zebiak, 1985; Battisti, 1988; Suarez and Schopf, 1988; Schopf and Suarez, 1988; Battisti and Hirst, 1989; Neelin, 1992; Philander *et al.*, 1992; Lau *et al.*, 1992; Jin 1997a,b). It is now recognized that warm SST anomalies in the central and eastern Pacific induce surface wind anomalies that gradually cause the

thermocline in the west to become elevated (Wyrtki, 1975). These induced thermocline perturbations in the west eventually progress eastward along the equator, elevating the thermocline in the eastern Pacific, initiating the cold (La Niña) phase of ENSO, and so on.

4.1 Description of ENSO simulation

An important step in a model-based investigation of ENSO is to evaluate the model's ability to simulate various observed aspects of ENSO. We shall now examine the ENSO cycle in the 43-year OGCM simulation. In order to extract the temperature variations associated with the ENSO signal, we perform a Principal Component / Empirical Orthogonal Function (PC/EOF) analysis of the SST simulated by the OGCM. The PC/EOF technique involves expanding a space-time field in terms of linearly independent orthogonal basic functions. This analysis provides percentage contributions to the total variance explained by the different linearly independent components. The spatial pattern of the first EOF of the OGCM simulated SST anomalies in the tropical Pacific is shown in Fig.7a. The corresponding EOF1 from the GISST and GFDLAD datasets are shown in Fig.7b and Fig.7c respectively. The time-series of the leading PC for the OGCM, GISST and GFDLAD datasets are shown in Figs.7(d-f). The first EOF shows a pattern of warm anomalies in the central and eastern tropical Pacific Ocean and negative anomalies in the equatorial west Pacific and the subtropics. The positive peaks in the PC1 time series correspond to the El Niño events of (1965, 1968, 1972, 1982, 1987, 1991, 1994, 1997) and the troughs correspond to the La Niña events of (1964, 1970, 1975, 1984, 1988, 1995, 1998) events (Trenberth, 1997). The irregular nature of ENSO can be seen from the PC1 time-series. Spectra of observed ENSO time-series have preferred time-scales that roughly correspond to 3-5 years (Neelin *et al.*, 1998). We have also seen that the PC1 time-series has broad spectral peaks around the 3-5 year time-scale. The correlation coefficient of the PC1 between the OGCM and GISST is 0.93 for the period (1958-2000) and the correlation of the PC1 between the OGCM and the GFDLAD dataset for the common period (1982-1999) is found to be 0.94. Thus the OGCM is consistent with the GISST and GFDLAD datasets in capturing the spatial and temporal variability of SST in the tropical Pacific.

4.2 Life cycle

The ENSO evolution in the OGCM can be examined by constructing the life cycle of ENSO using lagged linear regression analysis of the oceanic parameters from the 43-year simulation. The reference SST index for the regression analysis is the area-averaged SST over the NINO3.4 region (170°W - 120°W; 5°S -5°N). The NINO3.4 index and the PC1 index of SST (Fig.8d) are highly correlated ($r=0.91$). Figure.8 shows the regression of heat content anomalies versus the NINO3.4 SST index for various lags (-24 months to +24 months) at three-month intervals. This is similar to the regression analysis shown by Knutson *et al.*, (1997). The ocean heat content is computed by vertically integrating the temperature from surface to 500m. The regression patterns in Figs.8(a-c) show positive anomalies in the west Pacific and weak negative anomalies in the central-eastern Pacific. This stage corresponds to the piling up of warm waters in the west Pacific. This feature is consistent with the findings of Wyrtki (1975), who pointed out the accumulation of warm waters in the west Pacific about 2 years prior to the commencement of El Niño. The positive heat content anomaly spreads eastward in Figs.8(d-e). The warm near-equatorial anomaly in Fig.8f is flanked by negative anomalies around 15°N. An eastward migration of the positive anomaly from the equatorial central Pacific to the eastern Pacific Ocean can be noticed in Figs.8(f-g). This is accompanied by westward displacement of the off-equatorial negative anomalies as evident from Figs.8(f-g). The anomaly patterns at lags (-3, 0, +3, +6) show a striking east-west contrast that correspond to a mature El Niño phase. A gradual weakening of the east-west contrast starts from lag +9 onward. At this stage, the warm anomaly in the eastern Pacific separates into two off-equatorial anomalies which can be seen on either side of the equator in Fig.8i. An eastward propagation of the negative anomalies at the equator can be seen in Figs.8(l-m). As the cold anomalies intrude eastward, they replace the warm anomalies in the equatorial central-eastern Pacific leading to termination of the El Niño phase. The cold anomaly in the eastern equatorial Pacific intensifies in Figs.8(n-q). At the same time, the off-equatorial warm anomalies move westward and can be seen in the west Pacific in Figs.8(p-q). Note that the east-west anomaly pattern in Figs.8(p-q) has opposite polarity to that of the El Niño phase.

Lagged regression patterns of longitude-depth sections of potential temperature in the equatorial Pacific versus the NINO3.4 SST index are depicted in Fig.9. Starting

from a condition of warm (cold) anomaly in the western (eastern) Pacific, the subsurface anomalies from the west show a steady eastward propagation in Fig.9(a-f). The amplitude of the subsurface anomalies is maximum at a depth of around 125m. Around lag -6, the equatorial central-eastern Pacific ocean is replaced by positive anomalies and negative anomalies appear in the west Pacific. Thereafter, the El Niño condition gradually establishes so that the east-west contrast in the subsurface anomaly pattern intensifies in Figs.9(h-k). It can be noticed that the maxima in the subsurface anomalies is located in the main thermocline at depths between 50-250m. Following the establishment of the El Niño phase, the west Pacific cold anomalies in the subsurface gradually start propagating eastward as can be seen from Figs.9(j-m). The arrival of the cold subsurface anomalies in the eastern Pacific (Fig.9m) leads to increased upwelling and elevates the thermocline. This corresponds to the termination of the El Niño phase. As the cold subsurface anomalies develop in the central-eastern Pacific, the thermocline in the west Pacific is pushed downward resulting in accumulation of warm waters in the western part of the ocean basin. Thus the life cycle of the model ENSO as portrayed in Fig.8 and Fig.9 consistently bring out the point that the long-term memory of the phenomenon arises from the evolution of the subsurface ocean anomalies.

4.3 Physical interpretation of the model ENSO

From the above discussions, it is seen that the life cycle of ENSO in the OGCM is characterized by eastward propagating subsurface anomalies close to the equator and westward propagating anomalies away from the equator. Similar features have been seen in atmosphere/ocean coupled GCM simulations (Philander *et al.*, 1992; Lau *et al.*, 1992; Knutson *et al.*, 1997). According to the delayed oscillator mechanism (Battisti, 1988; Suarez and Schopf, 1988; Schopf and Suarez, 1988; Battisti and Hirst, 1989), a coupled instability develops in the central basin, in which a depressed thermocline produces anomalous SST warming. The warm SST results in anomalous westerly winds to the west of the warm patch, which further lowers the thermocline and the anomaly grows. The dynamical interpretation of this theory is based on the idea that the buildup of heat content in the western Pacific prior to the onset of El Niño (Wyrtki, 1975), is mediated by trade wind-forced downwelling equatorial Rossby waves. Reflection of Rossby waves off the western boundary can initiate El Niño events by generating downwelling equatorial Kelvin waves that

propagate eastward to cause warming in the equatorial cold tongue. Observed datasets have clearly documented equatorial Kelvin waves propagating eastward with phase speeds of $2-3 \text{ ms}^{-1}$ prior to and during the 1986-1987 El Niño (McPhaden *et al.*, 1998). Also there is observational evidence for equatorial Kelvin and Rossby waves associated with the 1991-93 El Niño warm event (Kessler and McPhaden, 1995).

More recently, Jin (1997 a,b) have produced a theoretical "recharge oscillator" paradigm to describe how changes in the volume of warm water are related to the timing of El Niño and La Niña events. In this theory, the depth of the main thermocline, and hence the volume of warm water above it, plays an important dynamical role in affecting the ENSO cycle by controlling the temperature of the waters upwelled in the eastern equatorial Pacific. Changes in the temperature of the upwelled waters in turn control the SST anomalies in the eastern equatorial Pacific, which then impact the zonal winds *via.*, changes in the patterns of deep atmospheric convection and sea level pressure gradients. The result is a positive feedback (SST gradients create anomalous winds and winds amplify SST gradient) in either the warm or cold phases of the ENSO cycle until enough water has been discharged from or recharged into the equatorial region to end the event. Observations provide confirmation that ENSO involves a recharge and discharge of warm water volume along the equator so as to influence the magnitude of the ENSO SST anomalies (Meinen and McPhaden, 2000).

Nevertheless, given the complexity of the observed interannual variability, tests of ENSO theories suggest that more than one set of mechanisms can give rise to ENSO time-scale warm and cold events in the tropical Pacific (McPhaden *et al.*, 1998). Moreover, there are considerable differences from one ENSO event to another. The availability of TAO moored buoy observations in the equatorial Pacific Ocean for the period (1992-2000) allows us to understand how the evolution of subsurface anomalies during the ENSO of (1997-99) differed from that of (1991-94). The plot in Fig.10a shows the longitude-time section of 20°C isotherm depth (ISO20) near the equator. It can be clearly seen from Fig.10a that the major El Niño of 1997 was associated with decrease in the ISO20 in the west Pacific and an increase in ISO20 to the east of the dateline. Note that the ISO20 depth shows a clear eastward propagation starting from early 1997 onward. The ISO20 maximum (155 m) is located around 150°W by September 1997. In contrast, the La Niña

phase which started from mid-1998 onward was characterized by a deepening (shoaling) of the thermocline in the west (east) Pacific respectively. An important aspect of the (1997-98) ENSO cycle was the fast switch over from a strong El Niño to a strong La Niña phase. This is evident from Fig.10b which shows the ISO20 averaged over the west Pacific (thin line) and east Pacific (thick line). The ISO20 depth in the west Pacific reveals a large decrease from about 200m in March 1997 to about 125m in December 1997. On the other hand, the ISO20 in the east Pacific shows a more gradual increase during the course of the 1997 El Niño. By December 1997, the ISO20 values in the west Pacific and east Pacific are found to be nearly at the same depth (~ 130 m). This condition was followed by a rapid fall (rise) of the ISO20 in the east (west) Pacific leading to the La Niña phase. Contrary to the fast phase reversals of the (1997-98) ENSO cycle, the El Niño conditions were more persistent and prolonged during (1991-94). The ISO20 in the west and east Pacific were more or less steadily maintained around 160m and 110m respectively (Fig.10c). Kessler and McPhaden (1995) analyzed observations from the TAO array and reported the appearance of equatorial Kelvin and Rossby waves associated with the (1991-93) El Niño warm event. They also pointed out that intraseasonal Kelvin waves were a prominent part of equatorial thermocline depth variability. However, the quick phase-reversals during the 1997-1998 was characterized by rapid upwelling changes and thermocline adjustments in the east and west Pacific (Mc Phaden, 1999).

The OGCM simulated upper ocean currents during the (1998-99) La Niña phase (Fig.11a) shows strong westward zonal currents in the top 50m and eastward undercurrents (below 75m). In addition, the simulated vertical velocity in Fig.11a is associated with strong upwelling ($\text{max} \sim 4 \text{ mm s}^{-1}$) stretching across the entire central-eastern equatorial Pacific. On the other hand, the westward surface currents seem to be practically absent with significantly weaker upwelling in the eastern Pacific during the (97-98) El Niño phase as seen from the OGCM simulation in Fig.11b. In fact, the vertical velocity shows prominent downwelling below 50m depth in the eastern Pacific (Fig.11b). The horizontal currents and vertical velocity associated with the prolonged El Niño of (1991-93) is shown in Fig.11c. By contrasting Fig.11b and Fig.11c, it can be noticed that the weakening of the surface currents and the reduction in upwelling were more pronounced during (1997-98) as compared to the (1991-93) El Niño. Thus the OGCM is consistent with TAO observations (Fig.10) in bringing out the point that the thermocline changes

associated with the dynamical evolution of the subsurface anomalies play an important role in determining the nature of individual ENSO events.

5 Meridional heat transport during ENSO

One of the issues relevant to our study is the heat transport variability associated with ENSO events. The plot in Fig.12a shows the warm minus cold (WMC) composite of the model simulated SST anomaly obtained from 7 El Niño and 7 La Niña events during (1958-2000). The corresponding wind-stress anomaly composite is superposed on the SST anomaly. The zonal extent of the warm anomaly in Fig.12a covers more than 60% of the tropical Pacific basin. The anomalous westerlies over this region correspond to a major weakening of the surface easterly trade winds in the tropical Pacific. The maxima in the SST and wind-stress anomalies in the equatorial central-eastern Pacific are co-located and indicate the importance of atmosphere-ocean coupling during ENSO events. Also note that the warm SST anomaly in the tropics is flanked by cold anomalies in the mid-latitude Pacific Ocean. The WMC composite of subsurface temperature (Fig.12b) shows that the anomalous warming in the equatorial central-eastern Pacific appears as deep as 150m from the surface. We have further verified that the simulated sea level increases in the tropical central-eastern Pacific Ocean due to mass accumulation of warm waters in the equatorial region during El Niño events (figure not shown). Energy balance considerations of the atmosphere-ocean system require that ocean dynamics must oppose the accumulation of heat in the equatorial region during ENSO events (Sun and Trenberth, 1998; Sun, 2000). In addition to heat removal, ocean dynamics must also redistribute the accumulated water mass in the equatorial Pacific. Sun (2000) carried out a diagnostic case study of observed datasets and noted that the surface heat fluxes pump heat into the equatorial ocean prior to the onset of El Niño. His results suggested that as El Niño develops, the heat stored in the subsurface ocean resurfaces in the eastern equatorial Pacific. He also noted that the excessive heat must be transported poleward from the equatorial ocean. However, it should be pointed out that the heat convergence in the upper ocean computed by Sun (2000) does not explicitly include ocean circulation dynamics. Moreover, in the heat pump theory of Sun (2000), the surface heat fluxes are the main forcing terms for pumping heat into the equatorial oceans prior to the commencement of El Niño. However,

it is important to point out that as the El Niño develops, there is significant build up of warm waters in the central and eastern equatorial Pacific Ocean due to ocean dynamical processes (Meinen and McPhaden, 2000). Hence, it is worthwhile to inquire as to how the ocean dynamics might respond so as to prevent the accumulation of heat and mass in the equatorial Pacific Ocean during El Niño events.

Much of the heat transport variability is due to wind-induced current fluctuations in which the time-varying wind stress drives the Ekman layer mass transports (Jayne and Marotzke, 2001). Numerical experiments conducted by Bryan (1982) showed that the seasonal variations of cross-equatorial heat transport largely depend on the zonal component of wind stress. Using the OGCM simulations, we now investigate the dynamical response of the ocean to ENSO forcing in terms of heat and mass transport variability. The dashed line in Fig.13 shows the latitudinal variation of the climatological heat transport in the Pacific Ocean averaged for 43 years (1958-2000). The thick line is the heat transport in the Pacific Ocean composited from 7 El Niño events. The thin line is the heat transport composite based on 7 La Niña events. It can be seen that the northward heat transport in the El Niño composite exceeds the 43-year time-mean heat transport in the (15°S - 15°N) latitude belt. The peak value in the El Niño composite is about 3.4 PW; the peak value for the 43-year mean is about 2.4 PW; while the peak value in the La Niña composite is about 2.1 PW. Note that the magnitude of change (relative to the 43-year mean) in the heat transport during El Niño is much larger than the corresponding magnitude of change during La Niña. This asymmetry between the warm and cold phases of the ENSO cycle implies differences in the relative importance of physical process determining the heat transport variations during El Niño and La Niña events.

In order to dynamically interpret the heat transport variability associated with ENSO, we now examine the changes in the meridional circulation. Figure.14a shows the WMC composite of the OGCM simulated meridional mass transport and current anomalies. The positive shading in Fig.14a shows an anomalous increase in the net northward mass transport that covers a wide region of the Pacific basin. The anomalous eastward currents close to the equator are associated with accumulation of warm water in the central-eastern Pacific Ocean during El Niño events. This is accompanied by anomalous northward currents at the eastern boundary and westward current anomalies around

9°N extending from the eastern Pacific upto the dateline. A more important feature in Fig.14a is the anomalous north-eastward currents that extend from the dateline towards the eastern boundary. This anomalous circulation weakens the subtropical gyre along the eastern boundary and reduces the equatorward flow of cold waters. The area-averaged volume transport for the central-eastern Pacific Ocean (180°E-90°W; 0-30°N) shows that the anomalous decrease of volume transport in the WMC composite is about 3.4 Sv (1 Sverdrup = $10^6 \text{ m}^3 \text{ s}^{-1}$). Furthermore, the anomalous northward currents are not just confined merely to the surface alone, but also extend into the subsurface as evident from the WMC composite of meridional circulation anomaly in the Y-Z plane (Fig.14b). The strong northward current anomalies in the ocean mixed layer correspond to an increase in the Ekman transport, which extends from the equator to about 15°N. In the subsurface (60-200m), the current anomalies extend further northward into the subtropics and midlatitudes. An anomalous increase in upwelling can be seen in the mid-latitude North Pacific (30-45°N). The increased mid-latitude upwelling in the OGCM simulation is interesting from the point of the anomalous cooling in the North Pacific associated with ENSO (see Fig.12a). Note that the near-surface ocean response in the mid-latitudes is associated with anomalous southward currents. Earlier studies have pointed out that changes in heat fluxes and surface wind variability near the Aleutian low are major contributors to the variability of SST and near-surface ocean currents in the North Pacific (Cayan, 1980; Deser and Blackmon, 1995; Knutson and Manabe, 1998). Besides the surface wind induced changes, it also appears from Fig.14b that enhanced upwelling in the North Pacific region could be an additional factor that contributes to the intensification of the cold anomalies in the mid-latitude region during El Niño events. In short, the results from Fig.14 clearly confirm that interannual changes associated with ENSO alters the meridional transport and the structure of currents in the upper ocean, thereby influencing the heat and mass transport in a significant manner.

There is now growing evidence indicating that the heat balance in the Pacific and Atlantic Oceans involves a meridional circulation cell extending from the subtropics to the equator (McCreary and Lu, 1994). The source waters of the Pacific equatorial under current are the tropical and subtropical cells associated with meridional circulations (McCreary and Lu, 1994; Lu *et al.*, 1998). Under normal conditions, the surface water in the subtropics subducts into the thermocline, flows equatorward in the subtropical gyre and

a part of it eventually moves into the equatorial Pacific forming a closed subtropical cell (McCreary and Lu, 1994). However, it appears that the meridional cell in the subtropics varies significantly during ENSO events as seen from the OGCM simulation. In particular, it can be noticed from Fig.14b that the subsurface current anomaly, extending northward into the subtropics, counteracts the subtropical subduction and weakens the equatorward transport of subsurface cold waters. This effect in turn can influence the magnitude of the ocean temperatures in the equatorial region during ENSO events. Further studies will be necessary in order to unravel the details of the meridional cell variability and its possible feedback on the ENSO dynamics.

6 Summary

Results of numerical simulation of a global OGCM are presented along with diagnostic analysis of multi-source oceanic datasets with a view to understand the time-mean structure and interannual variability of the tropical oceans. Validation of the model simulated time-mean response with observed datasets indicates that the climatological features and the associated seasonal evolution of ocean temperatures and the meridional heat transport are realistically captured by the OGCM. The interannual variability of the model response was examined in a 43-year (1958-2000) integration of the OGCM driven by atmospheric forcings computed from the NCEP reanalysis. The spatial and temporal variability of Pacific SST in the 43-year simulation clearly brings out the observed El Niño and La Niña events. Examination of the simulated interannual variability of ocean temperatures associated with ENSO reveals that the model simulation has good resemblance with observed datasets in capturing the evolution of thermocline perturbations in the Pacific Ocean.

The life cycle of the model ENSO is characterized by eastward propagating heat content anomalies close to the equator and westward propagating off-equatorial anomalies. The above evolution of subsurface anomalies is similar to those noted in earlier coupled modelling experiments (Philander *et al.*, 1992; Knutson *et al.* 1997). According to the delayed oscillator mechanism (Battisti, 1988; Suarez and Schopf, 1988; Schopf and Suarez, 1988; Battisti and Hirst, 1989), the evolution of ENSO is governed by interplay between large-scale equatorial ocean wave processes and ocean-atmosphere feedbacks. Alternatively, the recharge oscillator theory (Jin, 1997 a,b) emphasizes the point that the

recharge and discharge of warm waters along the equator controls the upwelling changes in the eastern Pacific and thereby influences the temperature anomalies in the region. Both these theories focus on the importance of coupled dynamics; but do not address the issue concerning the accumulation of excessive heat and mass in the equatorial Pacific Ocean during El Niño episodes.

Sun and Trenberth (1998) and Sun (2000) have proposed a heat pump hypothesis in which the coupled tropical ocean-atmosphere system exports the excessive heat from the equatorial region to the subtropics as the El Niño develops. The heat convergence in the upper ocean computed by Sun (2000) was based on a 1-dimensional energy balance model without explicit treatment of ocean internal dynamics. On the other hand, our OGCM simulation allows us to examine the dynamical changes in the meridional currents associated with heat transport variations during ENSO. It is seen that the simulated poleward heat transport in the equatorial Pacific Ocean increases by as much as 1.2 PW from its mean value during El Niño events. The warm subsurface temperature anomalies in the equatorial thermocline are accompanied by anomalous northward currents extending from the equatorial region to the subtropics and result in a weakening of the subtropical gyre along the eastern boundary. These anomalous northward currents in the thermocline are found to reduce the equatorward mass transport of colder subsurface water from the subtropics by as much as 3.4 Sv. The conclusive result emerging from this study highlights two points (a) First, the anomalous northward currents remove heat from the equatorial region (b) The reduction in the equatorward flow of cold waters from the subtropics counteracts the mass accumulation of warm waters transport along the equator. The question still remains as to whether the heat and mass transport variability can actually feedback on the ENSO evolution itself? Further research is required in order to understand the interactions between the equatorial and subtropical Pacific Oceans that can potentially affect the ENSO cycle.

Acknowledgments

This research work was supported by the Indian Ocean Modelling / Department of Ocean Development (DOD/INDOMOD) project funds. The authors thank Dr.Gangan Prathap and Mr.Thankavelu, CMMACS, Bangalore, for allowing them to use the SGI Orgin3000 computer system under the INDOMOD programme. Special acknowledgements are due

to Drs Philip W.Jones, Richard D.Smith and John Davis, LANL, USA, for their help in porting the OGCM. We thank Dr.V. Satyan, Director, WCRP/WMO (former Head, Climate and Global Modelling Division, Indian Institute of Tropical Meteorology, Pune, India) for supporting the ocean modelling activity. We are thankful to Dr.P. S. Salvekar for reviewing the manuscript and providing helpful comments. We thank Director, IITM, for providing the infrastructural facilities. Dr.Gufran Beig and Mrs. Suvarna Fadnavis were generous in letting us use the SGI workstation during the initial stages of model testing.

A Heat flux calculations

The OGCM was forced with the net surface heat flux (Q_{NET}), which is a sum of sensible heat flux (Q_S), latent heat flux (Q_L), Long wave flux (Q_{LW}) and short wave flux (Q_{SW}). The basic parameters [air-temperature (T_a) and specific humidity at 2 m (q_m), total cloud fraction (λ), net shortwave radiation at surface, wind speed (U) at 10m] are based on NCEP reanalysis. The SST (T_s) data for flux computation is taken from GISST2.3b. The fresh water flux forcing for the salinity equation is computed from the precipitation and evaporation rates from NCEP reanalysis. The flux computation is described below.

$$Q_S = c_p c_h U (T_s - (T_a + \gamma z)) \quad (1)$$

$$Q_L = LC_e U (q_s - q_a) \quad (2)$$

$$Q_{LW} = \epsilon \sigma_{SB} (0.39 - 0.05 e^{0.5}) (1 - \lambda n^2) T_s^4 + 4 \epsilon \sigma_{SB} T_s^3 (T_s - T_a) \quad (3)$$

$$Q_{NET} = Q_S + Q_L + Q_{LW} + Q_{SW} \quad (4)$$

B References

- Battisti, D. S., Dynamics and thermodynamics of a warming event in a atmosphere-ocean model, *J. Atmos. Sci.*, 46, 2889-2919, 1988.
- Battisti, D. S., and A. C. Hirst, Interannual variability in the tropical atmosphere / ocean system: Influence of the basic state, ocean geometry and nonlinearity, *J. Atmos. Sci.*, 46, 1687-1712, 1989.
- Bjerknes, J., Atmospheric teleconnections from the equatorial Pacific, *Mon. Wea. Rev.*, 97, 163-172, 1969.
- Bryan, K., Climate and the Ocean Circulation: III. The Ocean Model, *Mon. Wea. Rev.*, 97, 806-827, 1969.
- Bryan, K., Seasonal variation in meridional overturning and poleward heat transport in the Atlantic and Pacific Oceans: A Model study, *J. Mar. Res.*, 40, Supplement, 39-53, 1982.
- Cane, M. A., and S. E. Zebiak, A theory for El Niño and Southern Oscillation, *Science*, 228, 1084-1087, 1985.
- Cayan, R. D., Large-scale Relationships between Sea Surface Temperature and Surface Air Temperature, *Mon. Wea. Rev.*, 108, 1293-1301, 1980.
- Derber, J., and A. Rosati, A Global Data Assimilation System, *J. Phys. Oceanogr.*, 19, 1333-1347, 1989.
- Deser, C., and M. L. Blackmon, On the Relationship between Tropical and North Pacific Sea Surface Temperature Variations, *J. Climate*, 8, 1677-1680, 1995.
- Dukowicz, K. J., R. D. Smith and R. C. Malone, A Reformulation and Implementation of the Bryan-Cox-Semtner Ocean Model on the Connection Machine, *J. Atmos. and Oceanic Tech.*, 10, 195-208, 1993.
- Dukowicz, K. J., and R. D. Smith, Implicit free-surface method for the Bryan-Cox-Semtner Ocean Model *J. Geophys. Res.*, 99, 7991-8014, 1994.
- Fu, L.-L., and R. D. Smith, Global ocean circulation from satellite altimetry and high-resolution computer simulation, *Bull. Amer. Meteor. Soc.*, 77, 2625-2636, 1996.
- Hastenrath, S., On meridional heat transports in the world ocean, *J. Phys. Oceanogr.*, 12, 922-927, 1982.
- Hellerman, S., and M. Rosenstein, Normal monthly wind stress over world ocean with error estimates, *J. Phys. Oceanogr.*, 13, 1093-1104, 1983.
- Hirst, A. C., Unstable and damped equatorial modes in simple coupled ocean-atmosphere models, *J. Atmos. Sci.*, 45, 830-852, 1986.
- Hu D., Global-scale Water Masses, Meridional circulation, and Heat Transport Simulated with a Global Isopycnal Ocean Model, *J. Phys. Oceanogr.*, 27, 96-120, 1997.
- Huang, R. X., and B. Qiu, Three-dimensional structure of the wind-driven circulation in the subtropical North Pacific, *J. Phys. Oceanogr.*, 24, 1608-1622, 1994.
- Jayne, R. S., and J. Marotzke, The Dynamics of Ocean Heat Transport Variability, *Rev. Geophys.*, 39, 385-411, 2001.
- Jin, F.-F., An equatorial recharge paradigm for ENSO, I, Conceptual model, *J. Atmos. Sci.*, 54, 811-829, 1997a.
- Jin, F.-F., An equatorial recharge paradigm for ENSO, II, A stripped-down coupled model, *J. Atmos. Sci.*, 54, 830-845, 1997b.
- Johnson, C. G., and M. J. McPhaden, Interior pycnocline flow from the Subtropical to

- the Equatorial Pacific Ocean, *J. Phys. Oceanogr.*, **29**, 3073-3089, 1999.
- Keith, D. W., Meridional energy transport, uncertainty in zonal means, *Tellus*, **47A**, 1173-1179, 1995.
- Kalnay, E., M. Kanamitsu, R. Kistler, W. Collins, W. Deaven, L. Gandin, M. Iredell, S. Saha, G. White, J. Woollen, Y. Zhu, M. Chelliah, W. Ebisuzaki, W. Higgins, J. Janowiak, K.C. Mo, C. Ropelewski, J. Wang, A. Leetmaa, R. Reynolds, Jenne Roy and Dennis Joseph, The NCEP/NCAR 40-Year Reanalysis Project, *Bull. Amer. Meteor. Soc.*, **77**, 437-471, 1996.
- Kessler, W. S. and M. J. McPhaden, The 1991-93 El Niño in the central Pacific, *Deep-Sea Research II*, **42**, 295-333, 1995.
- Kistler, R., E. Kalnay, W. Collins, S. Saha, G. White, J. Woollen, M. Chelliah, W. Ebisuzaki, M. Kanamitsu, V. Kousky, H. van den Dool, R. Jenne and M. Fiorino, The NCEP-NCAR 50-Year Reanalysis: Monthly Means CD-ROM and Documentation, *Bull. Amer. Meteor. Soc.*, **82**, 247-268, 2001.
- Knutson, T. R., S. Manabe, and D. Gu, Simulated ENSO in a global coupled ocean-atmosphere model: Multidecadal amplitude modulation and CO₂ sensitivity, *J. Climate*, **10**, 138-161, 1997.
- Lau, N. C., S. G. H. Philander, and M. J. Nath, Simulation of El Niño/Southern Oscillation phenomena with a low-resolution, coupled general circulation model of the global ocean and atmosphere, *J. Climate*, **5**, 284-307, 1992.
- Lau, N.-C., Interactions between Global SST Anomalies and the Midlatitude Atmospheric Circulation, *Bull. Amer. Meteor. Soc.*, **78**, 21-33, 1997.
- Levitus, S., R. Burgett and T. P. Boyer, World Ocean Atlas 1994, Volume 2: Temperature NOAA Atlas NESDIS 3, U.S. Department of Commerce, Washington, D.C., 99 pp, 1994.
- Levitus, S., R. Burgett and T. P. Boyer, World Ocean Atlas 1994, Volume 3: Salinity NOAA Atlas NESDIS 3, U.S. Department of Commerce, Washington, D.C., 99 pp, 1994.
- Lu, P., J. P. McCreary Jr., and B. A. Klinger, Meridional circulation cells and the source waters of the Pacific equatorial undercurrent, *J. Phys. Oceanogr.*, **28**, 62-84, 1998.
- Lysne, J and C. Deser, Wind-Driven Thermocline Variability in the Pacific: A Model-Data Comparison, *J. Climate*, **15**, 829-845, 2002.
- Maltrud, M. E., R. D. Smith, A. J. Semtner and R. C. Malone, Global eddy-resolving ocean simulations driven by 1985-1995 atmospheric winds, *J. Geophys. Res.*, **103**, 30825-30853, 1998.
- McCreary, J. P., and P. Lu, On the interaction between the subtropical and equatorial ocean circulation: the subtropical cell, *J. Phys. Oceanogr.*, **24**, 466-497, 1994.
- McPhaden, M. J., A. J. Busalacchi, R. Cheney, J. -R. Donguy, K. S. Gage, D. Halpern, M. Ji, P. Julian, G. Meyers, G. T. Mitchum, P. P. Niiler, J. Picaut, R. W. Reynolds, N. Smith and K. Takeuchi, The tropical Ocean-global Atmosphere observing system: A decade of progress, *J. Geophys. Res.*, **103**, 14169-14240, 1998.
- McPhaden, M. J, Genesis and Evolution of the 1997-98 El Niño , *Science*, **283**, 950-954, 1999.
- Meehl A. G., W. M. Washington, and A. J. Semtner, Experiments with a Global Ocean Model Driven by Observed Atmospheric Forcing, *J. Phy. Oceanogr.*, **12**, 301-312, 1982.
- Meinen C. S. and M. J. McPhaden, Observations of Warm Water Volume Changes in the Equatorial Pacific and Their Relationship to El Niño and La Niña, *J. Climate*, **13**, 3551-3559, 2000.
- Neelin J. D., M. Latif, M. A. F. Allaart, M. A. Cane, U. Cubasch, W. L. Gates, P. R. Gent,

- M. Ghil, C. Gordon, N-C. Lau, C. R. Mechoso, G. A. Meehl, J. M. Oberhuber, S. G. H. Philander, P. S. Schopf, K. R. Sperber, A. Sterl, T. Tokioka, J. Tribbia, S. E. Zebiak, Tropical air-sea interaction in general circulation models, *Climate Dynamics*, 7, 73-104, 1992.
- Neelin J. D., D. S. Battisti, A. C. Hirst, F. F. Jin, Y. Wakata, T. Yamagata and S. Zebiak, ENSO theory, *J. Geophys. Res.*, 103, 14261-14290, 1998.
- Pacanowski, R. C., and S. G. H. Philander, Parameterization of vertical mixing in numerical models of tropical oceans, *J. Phys. Oceanogr.*, 11, 1443-1451, 1981.
- Philander, S. G. H., T. Yamagata, and R. C. Pacanowski, Unstable air-sea interactions in the tropics, *J. Atmos. Sci.*, 41, 604-613, 1984.
- Philander, S. G. H., R. C. Pacanowski, N. C. Lau and M. J. Nath, Simulation of ENSO with a global atmospheric GCM coupled to a high-resolution, tropical Pacific ocean GCM, *J. Climate*, 5, 308-329, 1992.
- Peixoto, J. P., and A. H. Oort, *Physics of Climate*, American Institute of Physics, 1992.
- Rayner, N. A., E. B. Horton, D. E. Parker, C. K. Folland and R. B. Hackett, Version 2.2 of the Global sea-Ice and Sea Surface Temperature Data Set, 1903-1994., *Climate Research Technical Note*, 74, 24619-24639, 1998.
- Ronca, R. E., and D. S. Battisti, Anomalous Sea Surface Temperatures and Local Air-Sea Energy Exchange on Intra-Annual Timescales in the Northeastern Subtropical Pacific, *J. Climate*, 10, 102-117, 1997.
- Schopf, P. S. and M. J. Suarez, Vacillations in a coupled ocean-atmosphere model, *J. Atmos. Sci.*, 45, 549-566, 1988.
- Semtner, A. J., and R. M. Chervin, A Simulation of the Global Ocean Circulation with Resolved Eddies, *J. Geophys. Res.*, 93, 15502-15522, 1988.
- Semtner, A. J., Modeling Ocean Circulation, *Science*, 269, 1379-1385, 1995.
- Smith R. D, J. K. Dukowicz and R. C. Malone, Parallel ocean general circulation modeling, *Physica D*, 60, 38-61, 1992.
- Smith R. D, M. E. Maltrud, F. O. Bryan, and M. W. Hect, Numerical Simulation of the North Atlantic Ocean at $\frac{1}{10}^\circ$, *J. Phy. Oce.*, 30, 1532-1561, 2000.
- Suarez, M. J., and P. S. Schopf, A delayed action oscillator for ENSO, *J. Atmos. Sci.*, 45, 3283-3287, 1988.
- Sun D.-Z., and K. E. Trenberth, Coordinated heat removal from the equatorial Pacific during the 1986-87 El Niño, *Geophys. Res. Lett.*, 25, 2659-2662, 1998.
- Sun D.-Z., The Heat Sources and Sinks of the 1986-87 El Niño, *J. Climate*, 13, 3533-3550, 2000.
- Trenberth, K. E., The definition of El Niño, *Bull. Amer. Meteor. Soc.*, 78, 2771-2777, 1997.
- Trenberth, K. E., and J. M. Caron, Estimates of meridional atmosphere and ocean heat transports, *J. Climate*, 13, 4358-4365, 2001.
- Vonder Harr, T. H., and A. H. Oort, New estimate of annual poleward energy transport by northern hemisphere oceans, *J. Phys. oceanogr.*, 3, 169-172, 1973.
- Wallace, J. M., E. M. Rasmusson, T. P. Mitchell, V. E. Kousky, E. S. Sarachik, and H. von Storch On the structure and evolution of ENSO-related climate variability in the tropical Pacific: Lessons from TOGA, *J. Geophys. Res.*, 103, 14241-14259, 1998.
- Wyrtki, K., El Niño - the dynamic response of the equatorial Pacific Ocean to atmospheric forcing, *J. Phys. Oceanogr.*, 5, 572-584, 1975.
- Wyrtki, K., Water displacements in the Pacific and the genesis of El Niño cycles, *J.*

Geophys. Res., 90, 7129-7132, 1985.

Yamagata, T., Stability of a simple air-sea coupled model in tropics, *Coupled Ocean-Atmosphere Models*, edited by J. C. J. Nihoul, *Elsevier Oceanogr. Ser.*, 40, pp 637-657, Elsevier, New York, 1985.

Zebiak, S. E., and M. A. Cane, A model El Niño Southern Oscillation, *Mon. Weather Rev.*, 115, 2262-2278, 1987.

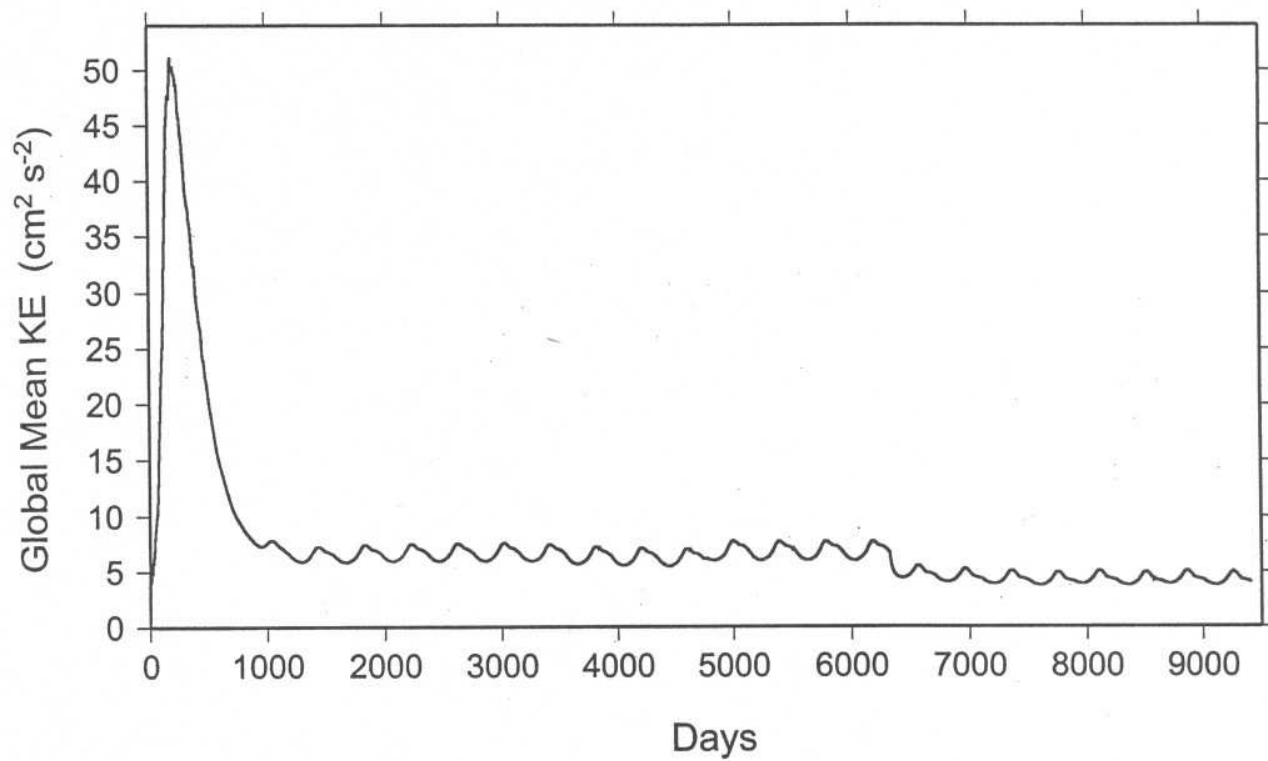


Figure 1: Time variation of global mean kinetic energy (cm²s⁻²) during the 24-year spin-up period.

SEA SURFACE TEMPERATURE

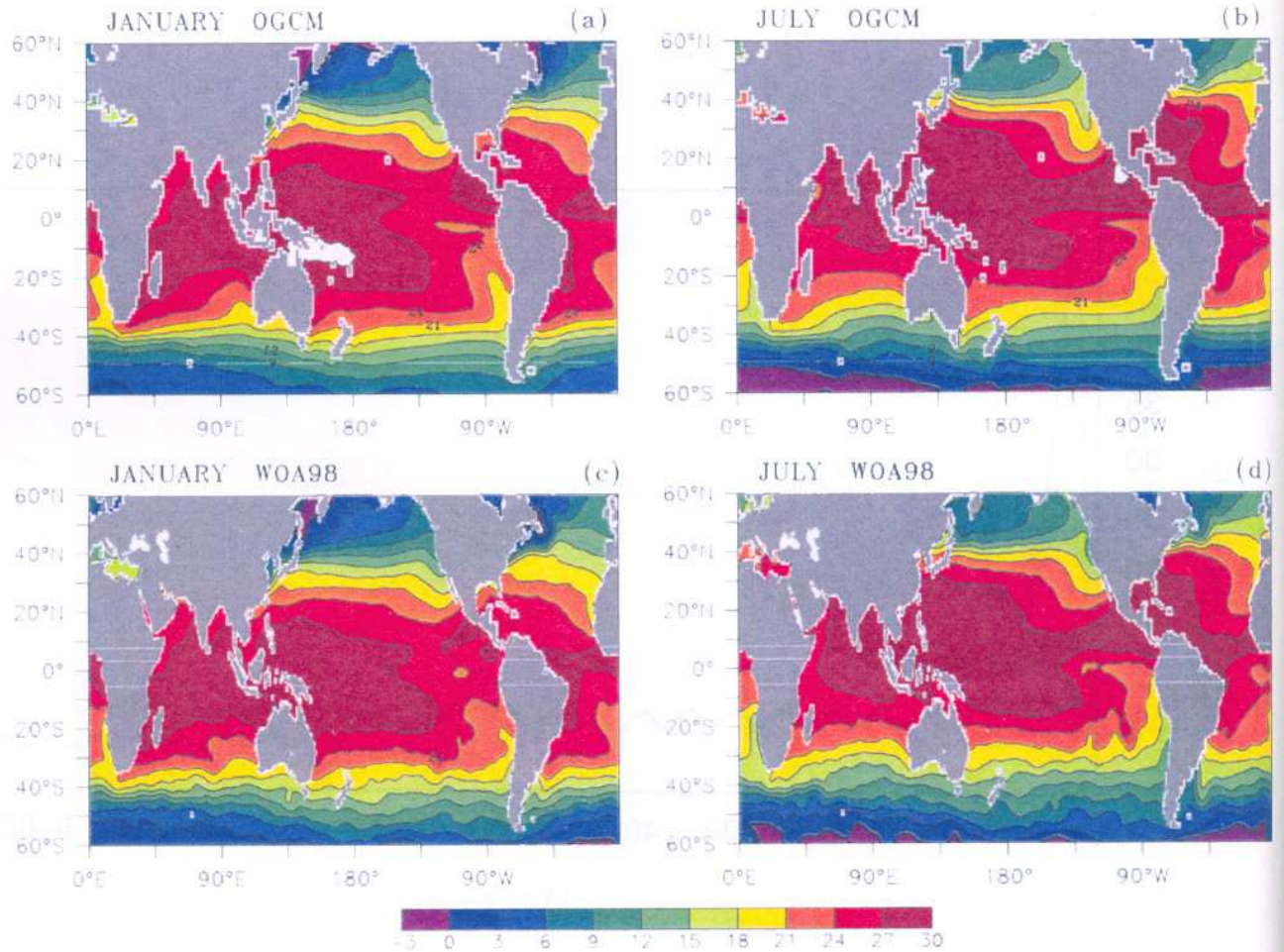


Figure 2 : Time-mean SST ($^{\circ}\text{C}$) (a) OGCM (January mean) (b) OGCM (July mean) (c) GFDLAD (January mean) (d) GFDLD (July mean)

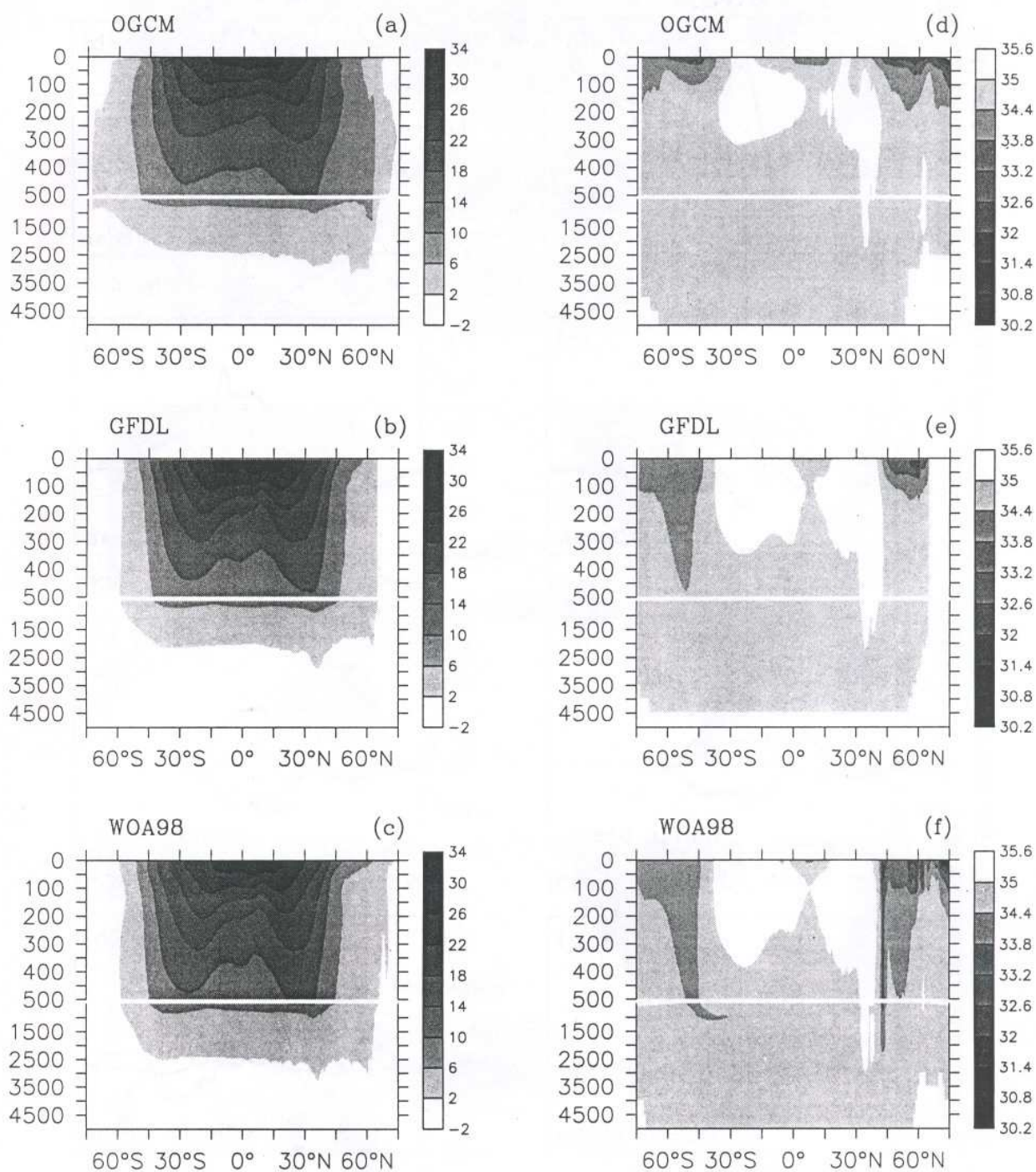


Figure 3: Zonally averaged potential temperature ($^{\circ}\text{C}$) shown in left column (a) OGCM (b) GFDLAD (c) WOA98. Zonally averaged salinity (psu) shown in right column (d) OGCM (e) GFDLAD (f) WOA98.

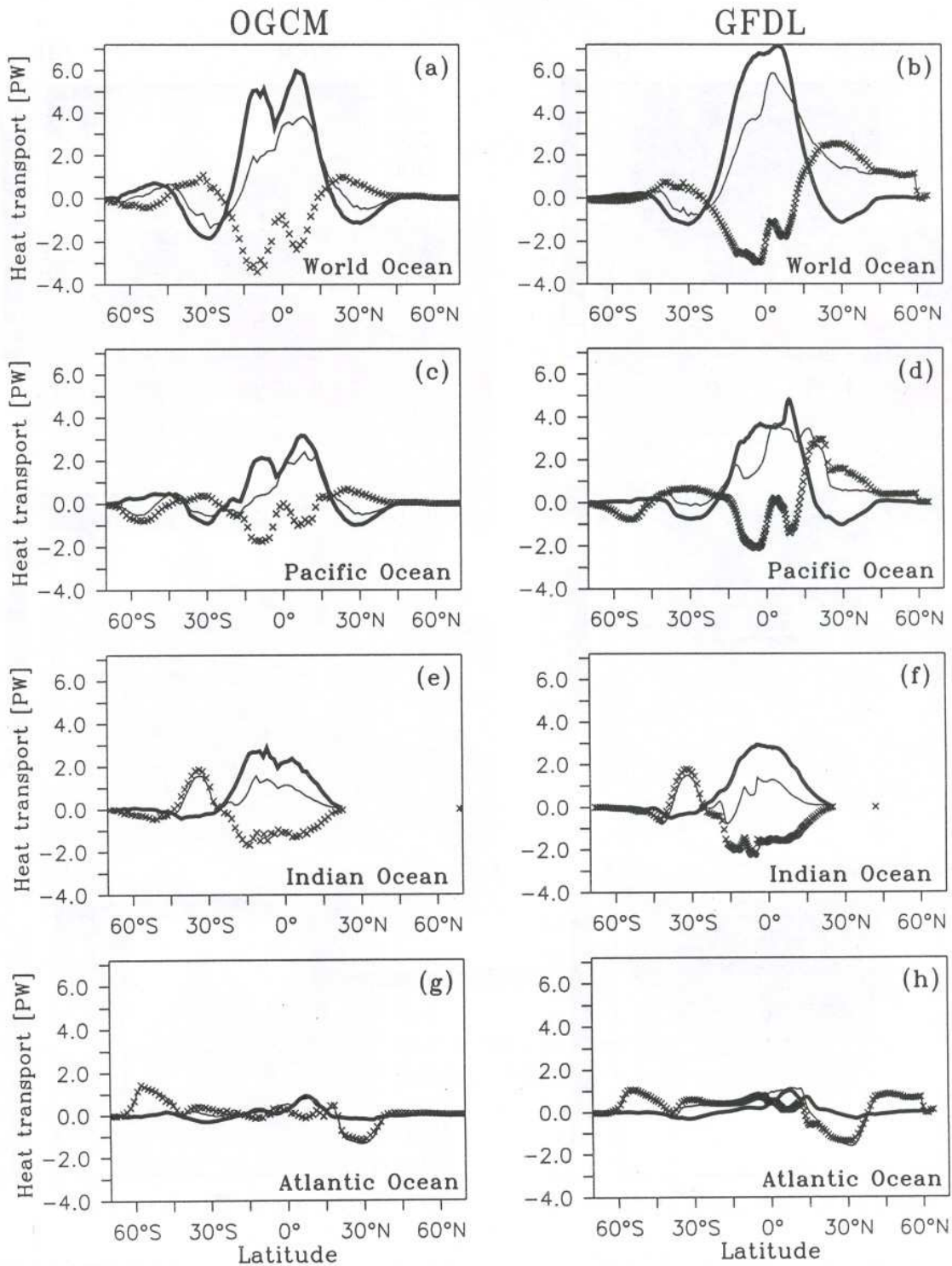


Figure 4: The meridional heat transport (PW) for different ocean basins computed from the OGCM (left column) and GFDL (right column). The meridional heat transport for January is shown by thin line and that for July is shown by asterisks. The annual cycle (January minus July) is shown by thick line. The zonal extent for the Pacific Ocean is (115°E-280°E); the Indian Ocean is (40°E-105°E) and the Atlantic Ocean is (68°W-16°E).

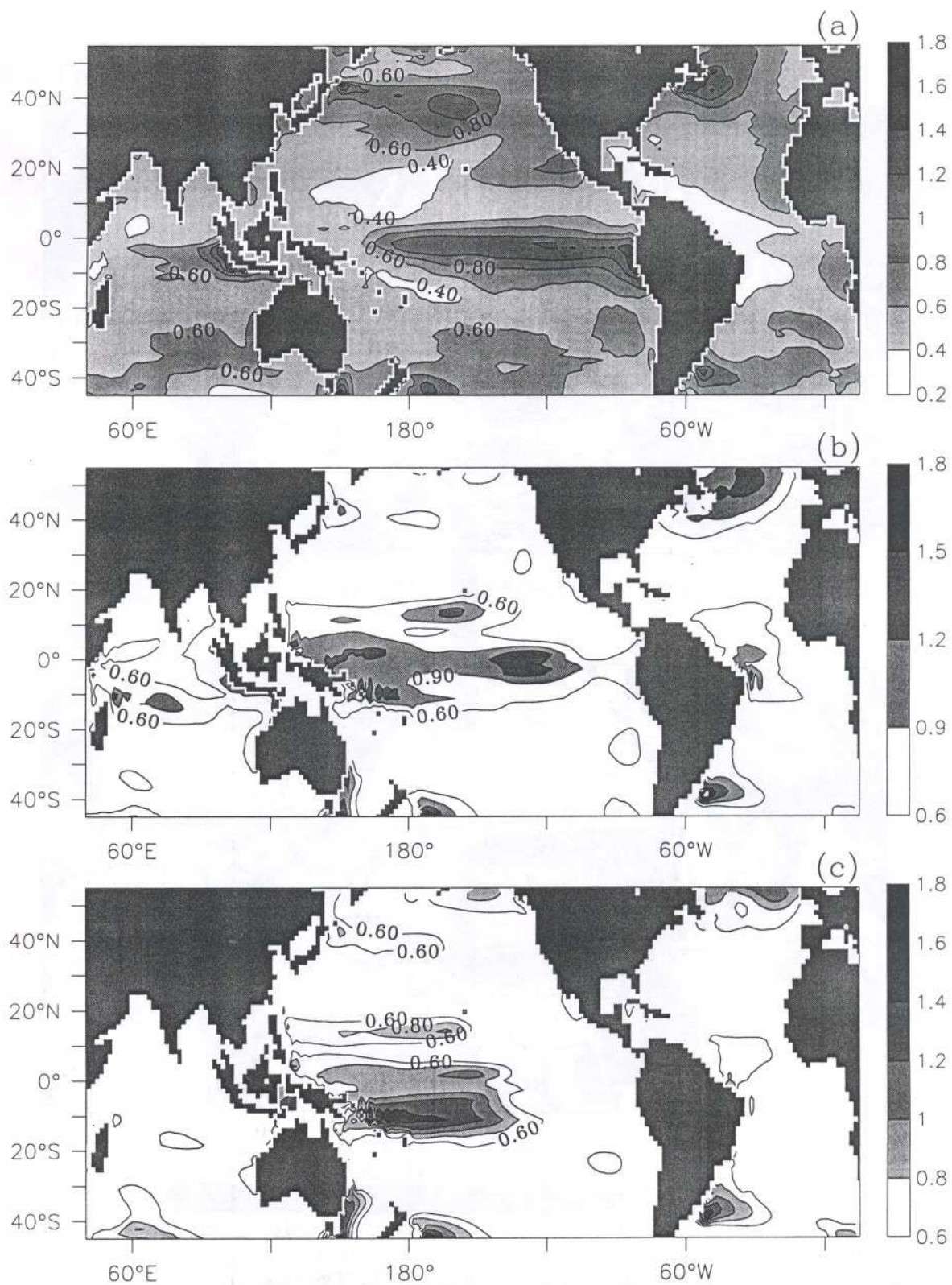


Figure 5: The standard deviation of the OGCM simulated potential temperature ($^{\circ}\text{C}$) from the 43-year run (a) 5 m (b) 100 m and (c) 150 m.

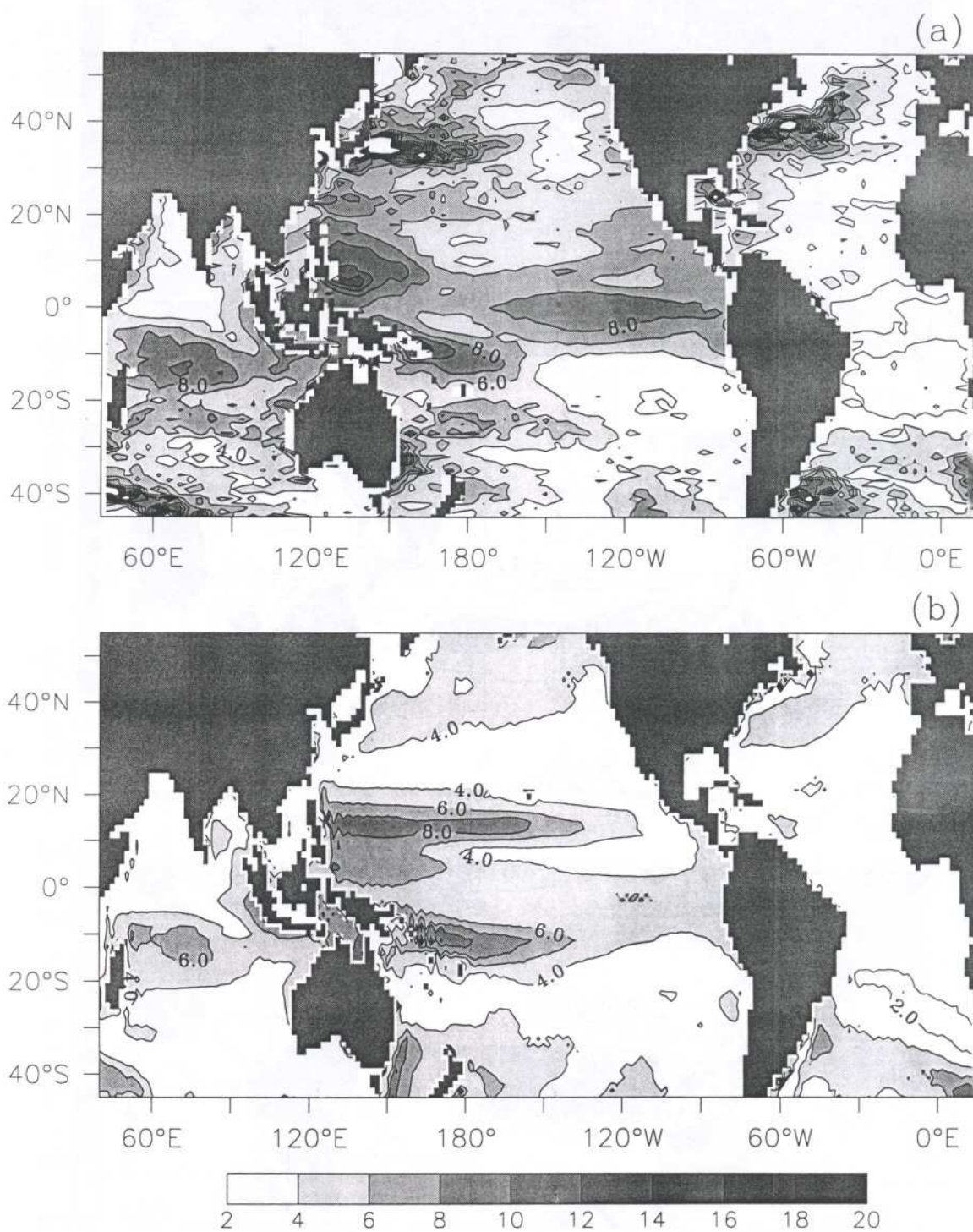


Figure 6: The standard deviation of SSH (cm) (a) TOPEX/POSEIDON dataset (1992-2000) (b) OGCM simulation (1958-2000).

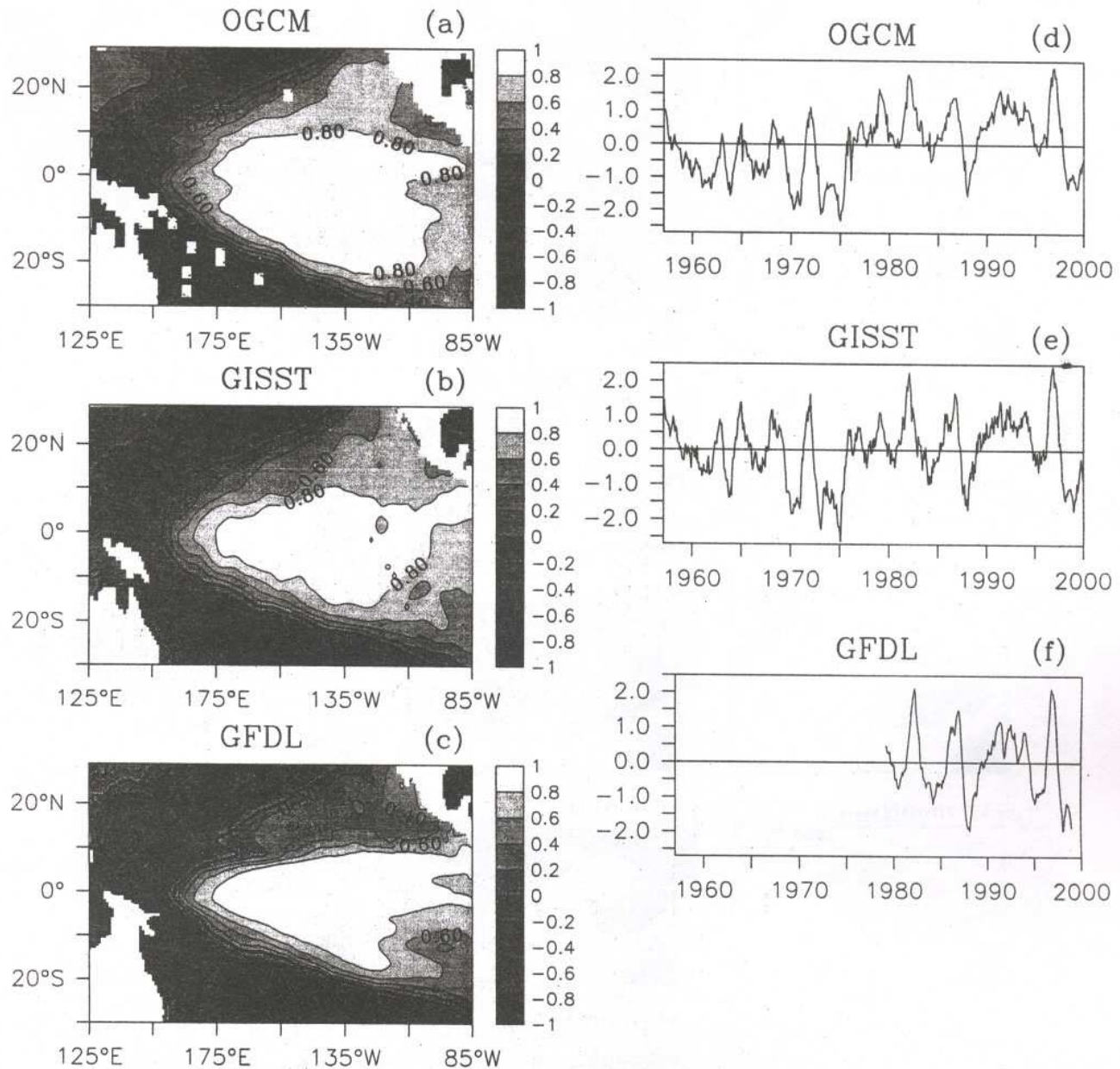


Figure 7: The spatial pattern of the first PC/EOF of SST shown for (a) OGCM simulation (1958-2000) (b) GISST dataset for the same 43-yr period (c) GFDLAD dataset (1980-1999). The corresponding time-series of the first PC shown in (d) OGCM simulation (e) GISST dataset (f) GFDLAD dataset. The variance explained by the first PC is about 32.1% of the total variance for the OGCM; 23.8% for the GISST and 36.0% for the GFDLAD dataset. Note that due to sparsity of SST observations during early periods, the GISST dataset relies on eigen vector reconstruction technique. For the OGCM and GFDLAD, the temperature at the 5m depth is taken as SST.



Figure 8 : Heat content anomaly life cycle, based on lagged regression of 5-500m vertically integrated heat content anomalies vs NINO3.4 SST (170°W-120°W, 5°S-5°N) from the 43-yr model simulation. The lag in months for each panel is displayed above the appropriate figure. Contour interval is 50m; values greater (less) than 25m (-25m) have dark (light) shading respectively

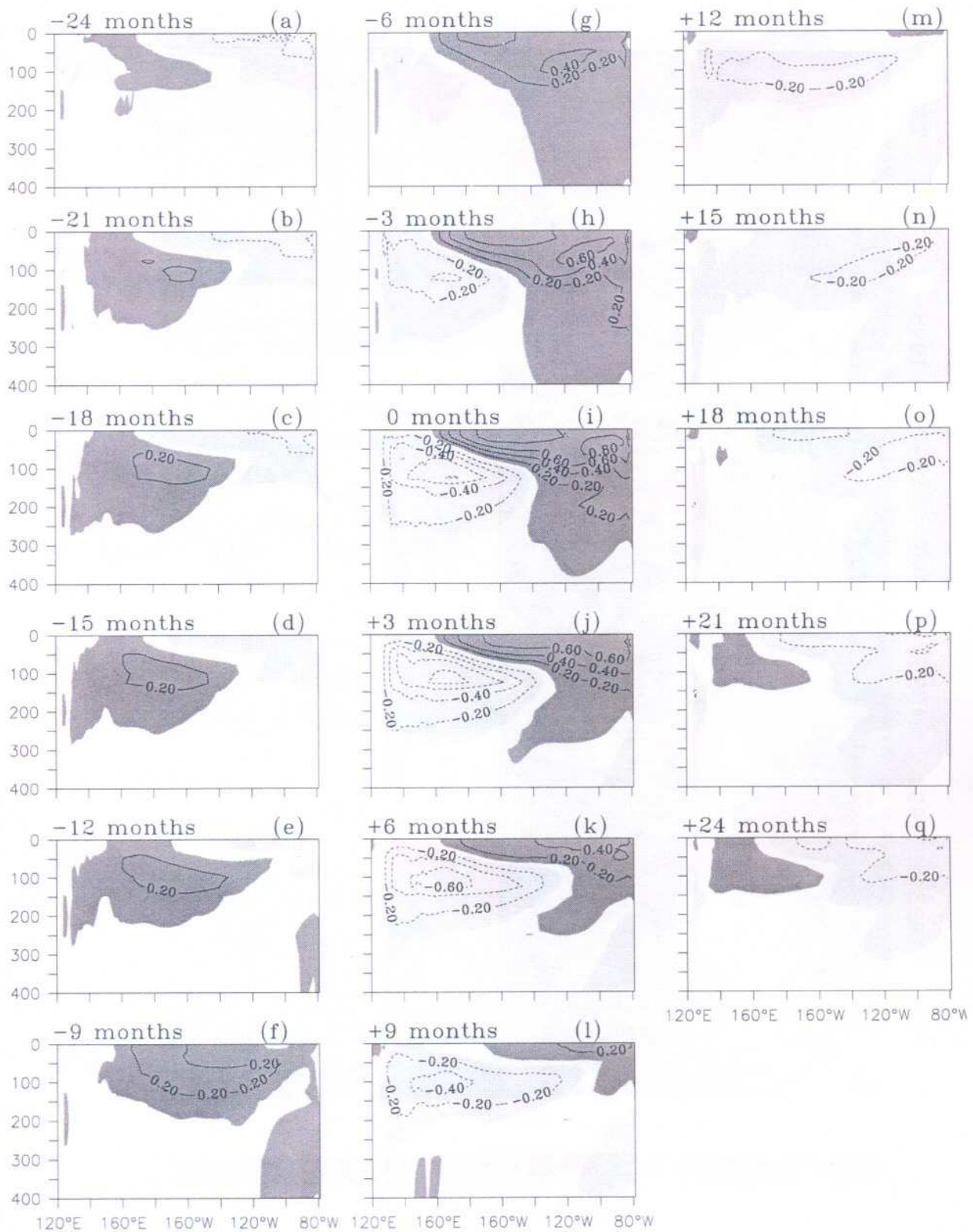


Figure 9 : As in Fig. 8, except for ocean temperatures averaged near the equatorial region (5°S - 5°N). The anomalies in each panel are function of depth (mete) and longitude. Contour interval is 0.2 (dimensionless); values greater (lesser) than 0.2 (-0.2) have dark (light) shading respectively

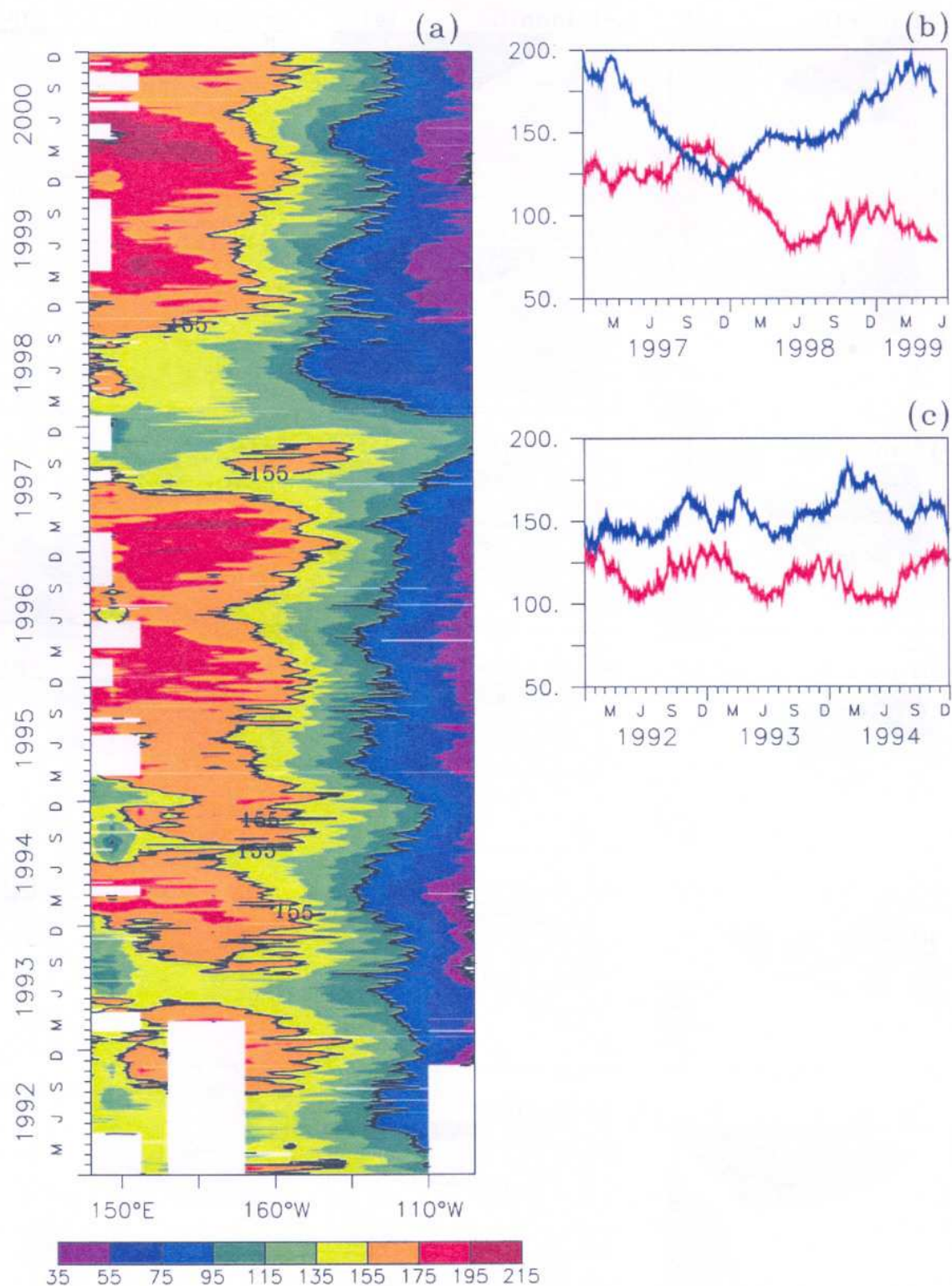


Figure 10 : (a) Time versus longitude section of ISO20(m) averaged between 8°S and 8°N (b) The area-averaged ISO20 (m) showing the 1997-99) ENSO cycle. The blue line is averaged for the equatorial western Pacific (137°E - 180°E , 8°S - 8°N) and the red line is averaged for the eastern Pacific (170°W - 100°W , 8°S - 8°N) (c) Same as (b) expect for the (1991-94) El Niño. The ISO20 data is based on measurements from the TAO moored buoys for the period (1992-2000)

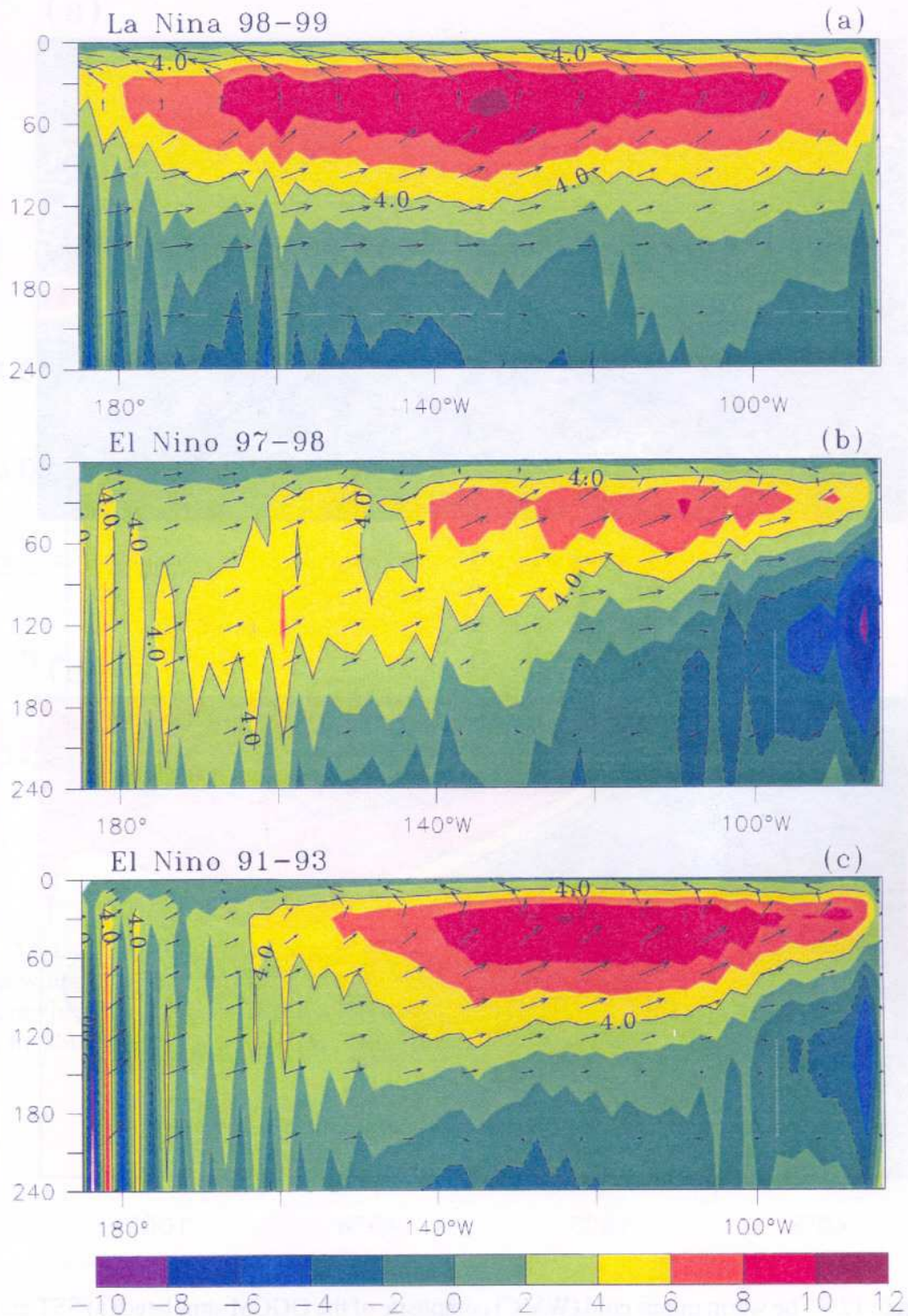


Figure 11 :Depth versus longitude section of OGCM simulated vertical velocity (shaded values) and vector currents in the equatorial region (5°S-5°N) for (a) La Niña phase (July 1998 - December 1999) (b) El Niño phase (April 1997 - April 1998) (c) El Niño (March 1991 - September 1993). The timings for these ENSO events based on Trenberth et al., (1997) The vertical velocity (cm s^{-1}) is scaled by a factor of 3×10^{-4}

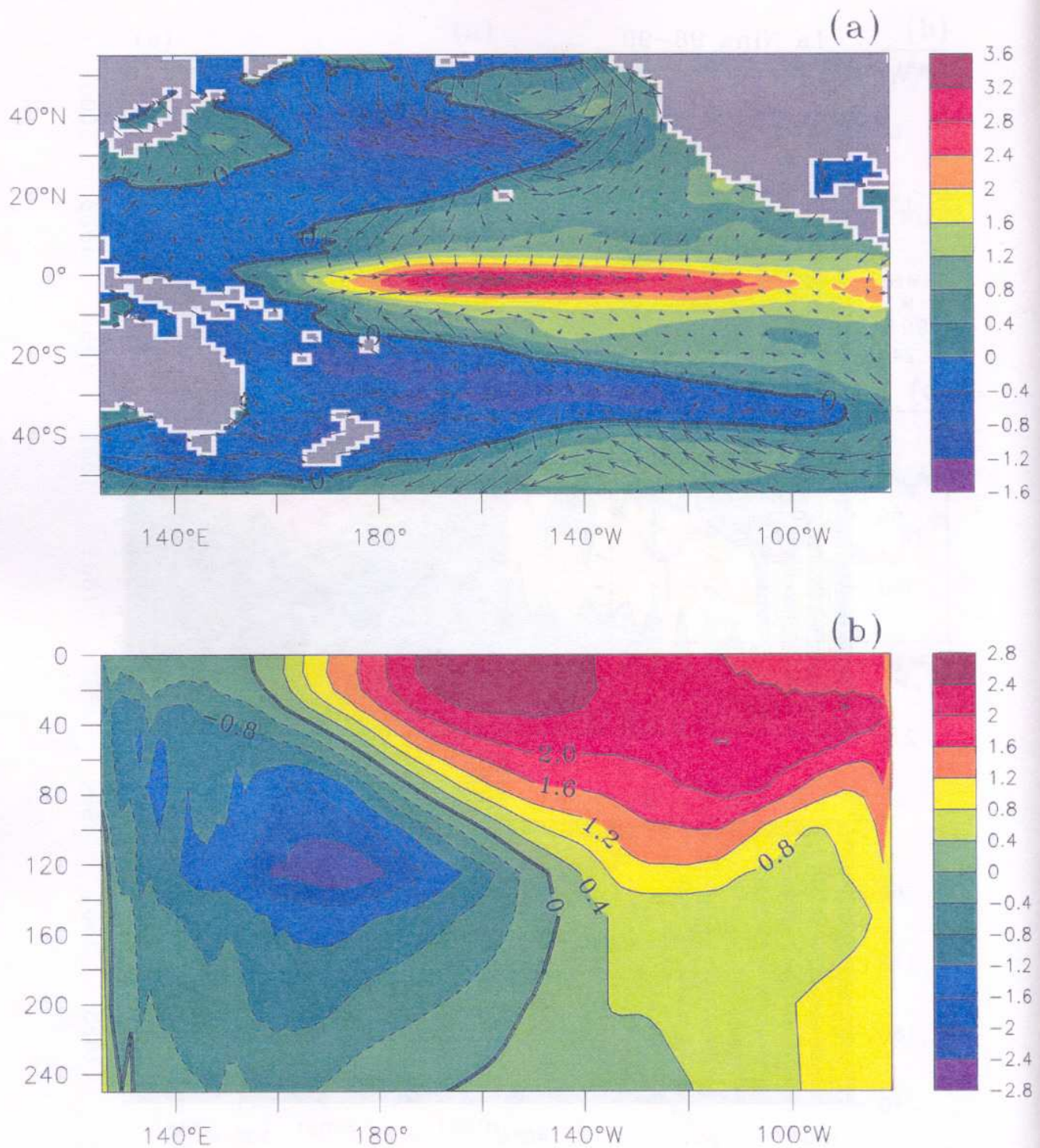


Figure 12 : The warm minus cold (WMC) composite of the OGCM simulated (a) SST anomalies with shading interval 0.9°C . The corresponding WMC composite of wind-stress anomalies (dynes cm^{-2}) from NECP reanalysis has been superposed (b) Longitude-depth section of potential temperature anomalies near the equator (5°S - 5°N). The shading interval $.8^{\circ}\text{C}$. The WMC composite are computed from the 7 El Niño and La Niña events given in fig. 12

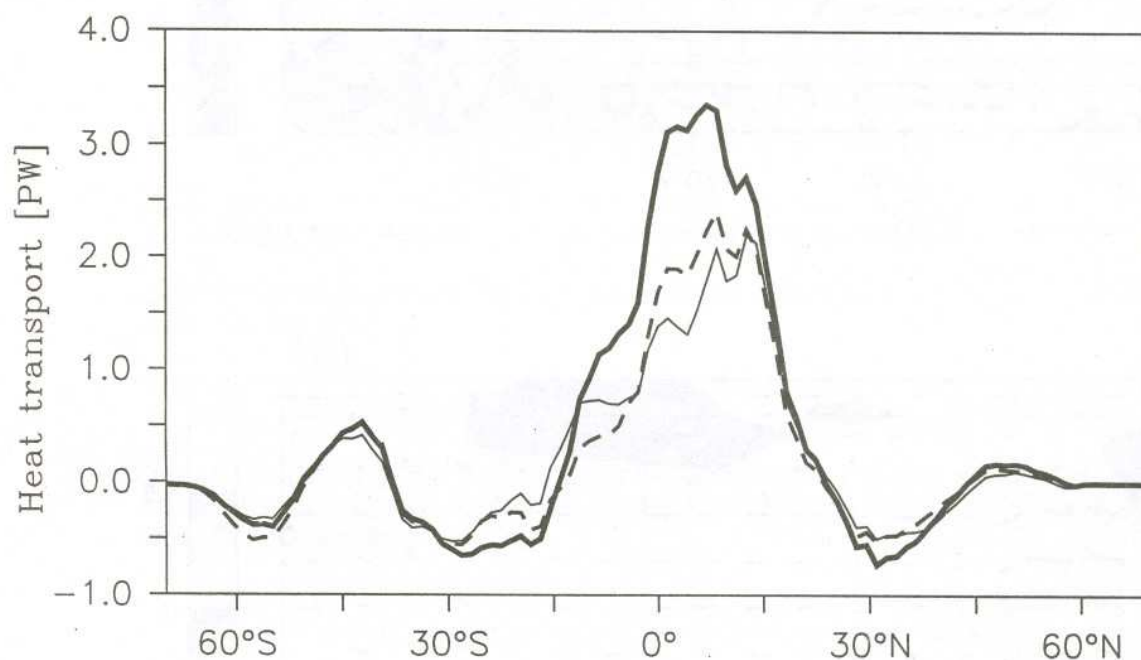


Figure 13: Latitudinal variation of meridional heat transport (PW) in the Pacific Ocean (115°E-280°E) during winter months (December - February) simulated by the OGCM. The dashed line is mean for 43-years; the thick solid line is the composite of 7 El Niño events (1965, 1968, 1972, 1982, 1987, 1991, 1997); the thin line is the composite of 7 La Niña events (1964, 1970, 1975, 1984, 1988, 1995, 1998).

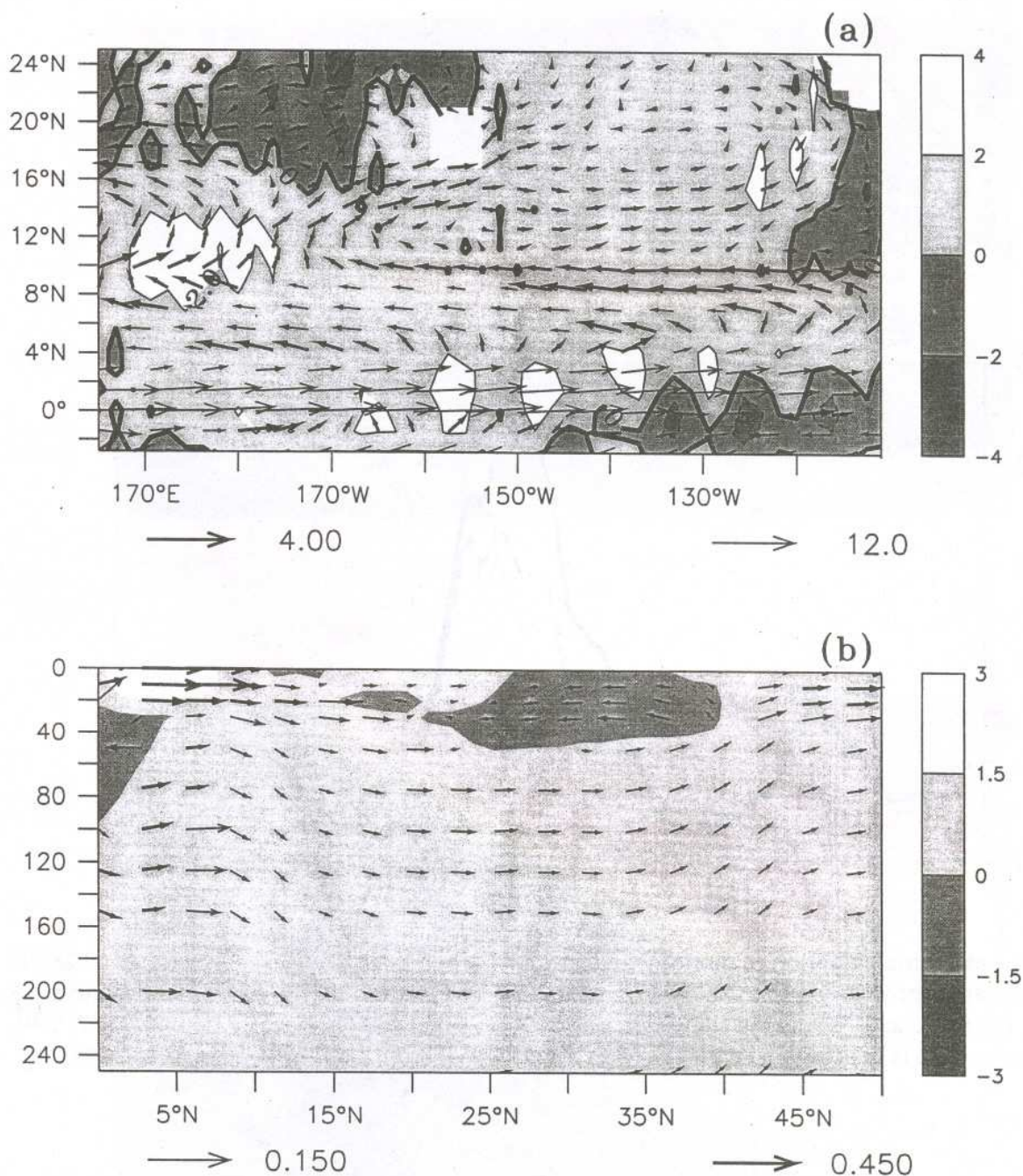


Figure 14: The warm minus cold (WMC) composite of the OGCM simulated (a) Mass transport (m^2s^{-1}) and current anomalies (cm/sec). The mass transport anomalies are computed by integrating the meridional velocity at the (5-1000m) depths. The current anomalies are averaged for the top 300m depths. (b) Depth-latitude section of meridional current anomalies averaged in the central-eastern Pacific (170°E-100°W). The anomalies of meridional velocity (cm s^{-1}) are shaded with interval 1.5 units. The magnitude of the current anomalies is much larger near the equator than in the subtropics. Therefore, thin and thick vectors are shown in order to avoid over-crowding near the equator.

I. I. T. M. RESEARCH REPORTS

- Energetic consistency of truncated models, *Asnani G.C.*, August 1971, RR-001.
- Note on the turbulent fluxes of heat and moisture in the boundary layer over the Arabian Sea, *Sinha S.*, August 1971, RR-002.
- Simulation of the spectral characteristics of the lower atmosphere by a simple electrical model and using it for prediction, *Sinha S.*, September 1971, RR-003.
- Study of potential evapo-transpiration over Andhra Pradesh, *Rakhecha P.R.*, September 1971, RR-004.
- Climatic cycles in India-1: Rainfall, *Jagannathan P. and Parthasarathy B.*, November 1971, RR-005.
- Tibetan anticyclone and tropical easterly jet, *Raghavan K.*, September 1972, RR-006.
- Theoretical study of mountain waves in Assam, *De U.S.*, February 1973, RR-007.
- Local fallout of radioactive debris from nuclear explosion in a monsoon atmosphere, *Saha K.R. and Sinha S.*, December 1972, RR-008.
- Mechanism for growth of tropical disturbances, *Asnani G.C. and Keshavamurty R.N.*, April 1973, RR-009.
- Note on "Applicability of quasi-geostrophic barotropic model in the tropics", *Asnani G.C.*, February 1973, RR-010.
- On the behaviour of the 24-hour pressure tendency oscillations on the surface of the earth, Part-I: Frequency analysis, Part-II: Spectrum analysis for tropical stations, *Misra B.M.*, December 1973, RR-011.
- On the behaviour of the 24 hour pressure tendency oscillations on the surface of the earth, Part-III : Spectrum analysis for the extra-tropical stations, *Misra B.M.*, July 1976, RR-011A.
- Dynamical parameters derived from analytical functions representing Indian monsoon flow, *Awade S.T. and Asnani G.C.*, November 1973, RR-012.
- Meridional circulation in summer monsoon of Southeast Asia, *Asnani G.C.*, November 1973, RR-014.
- Energy conversions during weak monsoon, *Keshavamurty R.N. and Awade S.T.*, August 1974, RR-015.
- Vertical motion in the Indian summer monsoon, *Awade S.T. and Keshavamurty R.N.*, August 1974, RR-016.
- Semi-annual pressure oscillation from sea level to 100mb in the northern hemisphere, *Asnani G.C. and Verma R.K.*, August 1974, RR-017.
- Suitable tables for application of gamma probability model to rainfall, *Mooley D.A.*, November 1974, RR-018.
- Annual and semi-annual thickness oscillation in the northern hemisphere, *Asnani G.C. and Verma R.K.*, January 1975, RR-020.

- Spherical harmonic analysis of the normal constant pressure charts in the northern hemisphere, *Awade S.T., Asnani G.C. and Keshavamurty R.N.*, May 1978, RR-021.
- Dynamical parameters derived from analytical function representing normal July zonal flow along 87.5 °E, *Awade S.T. and Asnani G.C.*, May 1978, RR-022.
- Study of trends and periodicities in the seasonal and annual rainfall of India, *Parthasarathy B. and Dhar O.N.*, July 1975, RR-023.
- Southern hemisphere influence on Indian rainfall, *Raghavan K., Paul D.K. and Upasani P.U.*, February 1976, RR-024.
- Climatic fluctuations over Indian region - Rainfall : A review, *Parthasarathy B. and Dhar O.N.*, May 1978, RR-025.
- Annual variation of meridional flux of sensible heat, *Verma R.K. and Asnani G.C.*, December 1978, RR-026.
- Poisson distribution and years of bad monsoon over India, *Mooley D.A. and Parthasarathy B.*, April 1980, RR-027.
- On accelerating the FFT of Cooley and Tukey, *Mishra S.K.*, February 1981, RR-028.
- Wind tunnel for simulation studies of the atmospheric boundary layer, *Sivaramakrishnan S.*, February 1981, RR-029.
- Hundred years of Karnataka rainfall, *Parthasarathy B. and Mooley D.A.*, March 1981, RR-030.
- Study of the anomalous thermal and wind patterns during early summer season of 1979 over the Afro-Asian region in relation to the large-scale performance of the monsoon over India, *Verma R.K. and Sikka D.R.*, March 1981, RR-031.
- Some aspects of oceanic ITCZ and its disturbances during the onset and established phase of summer monsoon studied with Monex-79 data, *Sikka D.R., Paul D.K. and Singh S.V.*, March 1981, RR-032.
- Modification of Palmer drought index, *Bhalme H.N. and Mooley D.A.*, March 1981, RR-033.
- Meteorological rocket payload for Menaka-II/Rohini 200 and its developmental details, *Vernekar K.G. and Brij Mohan*, April 1981, RR-034.
- Harmonic analysis of normal pentad rainfall of Indian stations, *Anathakrishnan R. and Pathan J.M.*, October 1981, RR-035.
- Pentad rainfall charts and space-time variations of rainfall over India and the adjoining areas, *Anathakrishnan R. and Pathan J.M.*, November 1981, RR-036.
- Dynamic effects of orography on the large scale motion of the atmosphere Part I : Zonal flow and elliptic barrier with maximum height of one km., *Bavadekar S.N. and Khaladkar R.M.*, January 1983, RR-037.
- Limited area five level primitive equation model, *Singh S.S.*, February 1983, RR-038.
- Developmental details of vortex and other aircraft thermometers, *Vernekar K.G., Brij Mohan and Srivastava S.*, November 1983, RR-039.

- Note on the preliminary results of integration of a five level P.E. model with westerly wind and low orography, *Bavadekar S.N., Khaladkar R.M., Bandyopadhyay A. and Seetaramayya P.*, November 1983, RR-040.
- Long-term variability of summer monsoon and climatic change, *Verma R.K., Subramaniam K. and Dugam S.S.*, December 1984, RR-041.
- Project report on multidimensional initialization for NWP models, *Sinha S.*, February 1989, RR-042.
- Numerical experiments with inclusion of orography in five level P.E. Model in pressure-coordinates for interhemispheric region, *Bavadekar S.N. and Khaladkar R.M.*, March 1989, RR-043.
- Application of a quasi-lagrangian regional model for monsoon prediction, *Singh S.S. and Bandyopadhyay A.*, July 1990, RR-044.
- High resolution UV-visible spectrometer for atmospheric studies, *Bose S., Trimbake H.N., Londhe A.L. and Jadhav D.B.*, January 1991, RR-045.
- Fortran-77 algorithm for cubic spline interpolation for regular and irregular grids, *Tandon M.K.*, November 1991, RR-046.
- Fortran algorithm for 2-dimensional harmonic analysis, *Tandon M.K.*, November 1991, RR-047.
- 500 hPa ridge and Indian summer monsoon rainfall : A detailed diagnostic study, *Krishna Kumar K., Rupa Kumar K. and Pant G.B.*, November 1991, RR-048.
- Documentation of the regional six level primitive equation model, *Singh S.S. and Vaidya S.S.*, February 1992, RR-049.
- Utilisation of magnetic tapes on ND-560 computer system, *Kripalani R.H. and Athale S.U.*, July 1992, RR-050.
- Spatial patterns of Indian summer monsoon rainfall for the period 1871-1990, *Kripalani R.H., Kulkarni A.A., Panchawagh N.V. and Singh S.V.*, August 1992, RR-051.
- FORTRAN algorithm for divergent and rotational wind fields, *Tandon M.K.*, November 1992, RR-052.
- Construction and analysis of all-India summer monsoon rainfall series for the longest instrumental period: 1813-1991, *Sontakke N.A., Pant G.B. and Singh N.*, October 1992, RR-053.
- Some aspects of solar radiation, *Tandon M.K.*, February 1993, RR-054.
- Design of a stepper motor driver circuit for use in the moving platform, *Dharmaraj T. and Vernekar K.G.*, July 1993, RR-055.
- Experimental set-up to estimate the heat budget near the land surface interface, *Vernekar K.G., Saxena S., Pillai J.S., Murthy B.S., Dharmaraj T. and Brij Mohan.*, July 1993, RR-056.
- Identification of self-organized criticality in atmospheric total ozone variability, *Selvam A.M. and Radhamani M.*, July 1993, RR-057.

- Deterministic chaos and numerical weather prediction, *Selvam A.M.*, February 1994, RR-058.
- Evaluation of a limited area model forecasts, *Singh S.S., Vaidya S.S Bandyopadhyay A., Kulkarni A.A, Bawiskar S.M., Sanjay J., Trivedi D.K. and Iyer U.*, October 1994, RR-059.
- Signatures of a universal spectrum for atmospheric interannual variability in COADS temperature time series, *Selvam A.M., Joshi R.R. and Vijayakumar R.*, October 1994, RR-060.
- Identification of self-organized criticality in the interannual variability of global surface temperature, *Selvam A.M. and Radhamani M.*, October 1994, RR-061.
- Identification of a universal spectrum for nonlinear variability of solar-geophysical parameters, *Selvam A.M., Kulkarni M.K., Pethkar J.S. and Vijayakumar R.*, October 1994, RR-062.
- Universal spectrum for fluxes of energetic charged particles from the earth's magnetosphere, *Selvam A.M. and Radhamani M.*, June 1995, RR-063.
- Estimation of nonlinear kinetic energy exchanges into individual triad interactions in the frequency domain by use of the cross-spectral technique, *Chakraborty D.R.*, August 1995, RR-064.
- Monthly and seasonal rainfall series for all-India homogeneous regions and meteorological subdivisions: 1871-1994, *Parthasarathy B., Munot A.A. and Kothawale D.R.*, August 1995, RR-065.
- Thermodynamics of the mixing processes in the atmospheric boundary layer over Pune during summer monsoon season, *Morwal S.B. and Parasnis S.S.*, March 1996, RR-066.
- Instrumental period rainfall series of the Indian region: A documentation, *Singh N. and Sontakke N.A.*, March 1996, RR-067.
- Some numerical experiments on roundoff-error growth in finite precision numerical computation, *Fadnavis S.*, May 1996, RR-068.
- Fractal nature of MONTBLEX time series data, *Selvam A.M. and Sapre V.V.*, May 1996, RR-069.
- Homogeneous regional summer monsoon rainfall over India: Interannual variability and teleconnections, *Parthasarathy B., Rupa Kumar K. and Munot A.A.*, May 1996, RR-070.
- Universal spectrum for sunspot number variability, *Selvam A.M. and Radhamani M.*, November 1996, RR-071.
- Development of simple reduced gravity ocean model for the study of upper north Indian ocean, *Behera S.K. and Salvekar P.S.*, November 1996, RR-072.
- Study of circadian rhythm and meteorological factors influencing acute myocardial infarction, *Selvam A.M., Sen D. and Mody S.M.S.*, April 1997, RR-073.
- Signatures of universal spectrum for atmospheric gravity waves in southern oscillation index time series, *Selvam A.M., Kulkarni M.K., Pethkar J.S. and Vijayakumar R.*, December 1997, RR-074.

- Some example of X-Y plots on Silicon Graphics, *Selvam A.M., Fadnavis S. and Gharge S.P.*, May 1998, RR-075.
- Simulation of monsoon transient disturbances in a GCM, *Ashok K., Soman M.K. and Satyan V.*, August 1998, RR-076.
- Universal spectrum for intraseasonal variability in TOGA temperature time series, *Selvam A.M., Radhamani M., Fadnavis S. and Tinmaker M.I.R.*, August 1998, RR-077.
- One dimensional model of atmospheric boundary layer, *Parasnis S.S., Kulkarni M.K., Arulraj S. and Vernekar K.G.*, February 1999, RR-078.
- Diagnostic model of the surface boundary layer - A new approach, *Sinha S.*, February 1999, RR-079.
- Computation of thermal properties of surface soil from energy balance equation using force - restore method, *Sinha S.*, February 1999, RR-080.
- Fractal nature of TOGA temperature time series, *Selvam A.M. and Sapre V.V.*, February 1999, RR-081.
- Evolution of convective boundary layer over the Deccan Plateau during summer monsoon, *Parasnis S.S.*, February 1999, RR-082.
- Self-organized criticality in daily incidence of acute myocardial infarction, *Selvam A.M., Sen D., and Mody S.M.S.*, February 1999, RR-083.
- Monsoon simulation of 1991 and 1994 by GCM : Sensitivity to SST distribution, *Ashrit R.G., Mandke S.K. and Soman M.K.*, March 1999, RR-084.
- Numerical investigation on wind induced interannual variability of the north Indian Ocean SST, *Behera S.K., Salvekar P.S. and Ganer D.W.*, April 1999, RR-085.
- On step mountain eta model, *Mukhopadhyay P., Vaidya S.S., Sanjay J. and Singh S.S.*, October 1999, RR-086.
- Land surface processes experiment in the Sabarmati river basin: an overview and early results, *Vernekar K.G., Sinha S., Sadani L.K., Sivaramakrishnan S., Parasnis S.S., Brij Mohan, Saxena S., Dharamraj T., Pillai, J.S., Murthy B.S., Debaje, S.B., Patil, M.N. and Singh A.B.*, November 1999, RR-087.
- Reduction of AGCM systematic error by Artificial Neural Network: A new approach for dynamical seasonal prediction of Indian summer monsoon rainfall, *Sahai A.K. and Satyan V.*, December 2000, RR-088.
- Ensemble GCM simulations of the contrasting Indian summer monsoons of the 1987 and 1988, *Mujumdar M. and Krishnan R.*, February 2001, RR-089.
- Aerosol measurements using lidar and radiometers at Pune during INDOEX field phases, *Mahes Kumar R.S., Devara P.C.S., Raj P.E., Jaya Rao Y., Pandithurai G., Dani K.K., Saha S.K., Sonbawne S.M. and Tiwari Y.K.*, December 2001, RR-090.
- Modelling studies of the 2000 Indian summer monsoon and extended analysis, *Krishnan R., Mujumdar M., Vaidya V., Ramesh K.V. and Satyan V.*, December 2001, RR-091.

- Intercomparison of Asian summer monsoon 1997 simulated by atmospheric general circulation models, *Mandke S.K., Ramesh K.V. and Satyan V.*, December 2001, RR-092.
- Prospects of prediction of Indian summer monsoon rainfall using global SST anomalies, *Sahai A.K, Grimm A.M., Satyan V. and Pant G.B.*, April 2002, RR-093.
- Estimation of nonlinear heat and momentum transfer in the frequency domain by the use of frequency co-spectra and cross-bispectra, *Chakraborty D.R. and Biswas M.K.*, August 2002, RR-094
- Real time simulations of surface circulations by a simple ocean model, *P Rahul Chand Reddy, Salvekar P.S., Ganer D.W. and Deo A.A.*, January 2003, RR-095
- Evidence of twin gyres in the Indian ocean : new insights using reduced gravity model by daily winds, *P Rahul Chand Reddy, Salvekar P.S., Ganer D.W. and Deo A.A.*, February 2003, RR-096
- Dynamical seasonal prediction experiments of the Indian summer monsoon, *Millind Mujumdar, R. Krishnan and V. Satyan*, June 2003, RR-097
- Thermodynamics and dynamics of the upper ocean mixed layer in the central and eastern Arabian sea, *C. Gnanaseelan, A.K. Mishra, Bijoy Thompson and P.S. Salvekar*, August 2003, RR-098
- Measurement of profiles and surface energy fluxes on the west coast of India at Vasco-Da-Gama, Goa during ARMEX 2002-03, *S. Sivaramakrishnan, B.S. Murthy, T. Dharmaraj, Cini Sukumaran and T. Rajitha Madhu Priya*, August 2003, RR-099